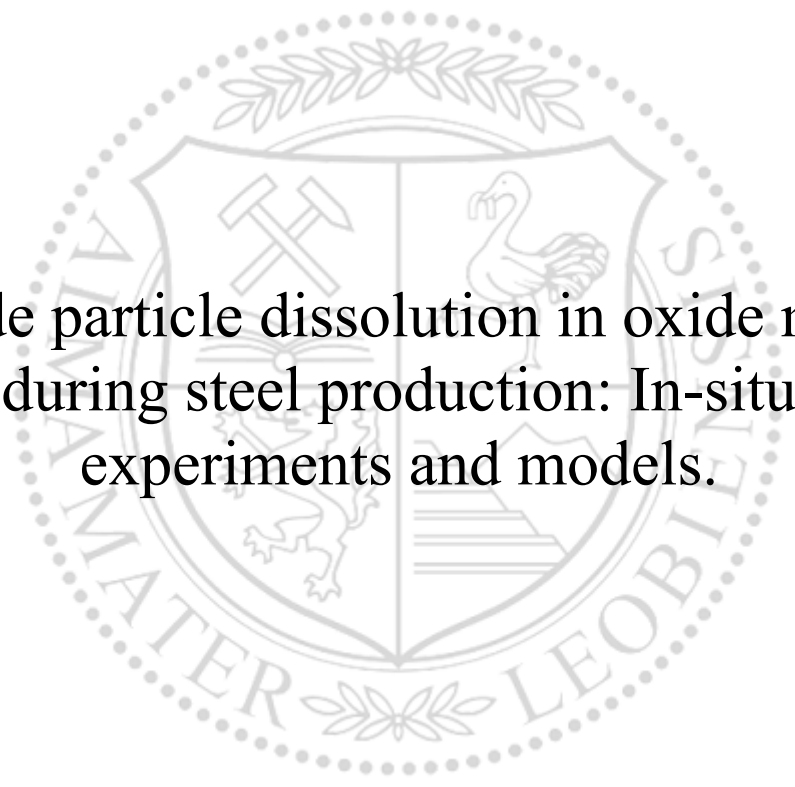




Chair of Mechanics

Master's Thesis



Oxide particle dissolution in oxide melts
during steel production: In-situ
experiments and models.

Oghenerukevwe Eru

August 2022



AFFIDAVIT

I declare on oath that I wrote this thesis independently, did not use other than the specified sources and aids, and did not otherwise use any unauthorized aids.

I declare that I have read, understood, and complied with the guidelines of the senate of the Montanuniversität Leoben for "Good Scientific Practice".

Furthermore, I declare that the electronic and printed version of the submitted thesis are identical, both, formally and with regard to content.

Date 24.11.2023

Signature Author
Oghenerukevwe Eru

Foreword

I will love to dedicate this research work to my late grandmother, Mrs Mary M. Aggreh, for her dedication and interest in my studies from my cradle and insisted on my travel to Austria for my graduate studies.

My special thanks go to Prof. Bart Blanplain, Prof. Johannes Schenk, Prof. Maria Seo, Prof. Stefan Steinlechner, and other members of the Co-ordinating Board of the EIT-SUMA programme for their vision and drive to make the SUMA program to become challenging and bring out the best out of its students. Combining studies at two of the partners (Montanuniversitaet Leoben, Austria and KU Leuven, Belgium) opened my eyes to new vistas in area of circularity.

Also, I thank K1-MET, Leoben and the Institute of Mechanics, Montanuniversitaet Leoben for the creation and funding of my thesis topic in the area of slag engineering, an area to which I was introduced to by Prof. Harald Raupenstrauch and Dr. Christof Ponak of the Chair for Thermal Process Technology, Montanuniversitaet Leoben. I am grateful for the knowledge gained from them.

Finally, my unreserved gratitude goes to my thesis supervisors (Prof. Bart Blanplain and Assoc. Prof. Ernst Gamsjäger), mentor (Dipl. In. Daniel Ogris) and the Christian Doppler Laboratory for Inclusion Metallurgy in Advanced Steelmaking (Assoz. Prof. Susanne Michelic and Jannik Wiesel) for their assistance during the preparation of this thesis, ranging from draft correction, experimentation to the series of the brain storming meetings that contributed to this milestone.

Oghenerukevwe Eru

Abstract

The dissolution of oxide particles is important for steel inclusion metallurgy due to the interaction between the refractory material and liquid steel, as well as in the area of steel cleanliness. It is affected by various factors which include the oxide particle's morphology (size and shape), the process's temperature, and the slag's composition.

In this study, the dissolution behaviour of oxide particles is investigated via a series of dissolution experiments. The dissolution of three different oxide particles (i.e., silica (SiO_2), alumina (Al_2O_3), and magnesium aluminate (MgAl_2O_4)) are observed in pre-melted $\text{CaO}-\text{Al}_2\text{O}_3-\text{SiO}_2$ slags (of varying composition) with the aid of a High-Temperature Laser Scanning Confocal Microscopy (HT-CLSM) setup.

The change in the diameter of the spherical oxide particles and the characteristic dissolution time is derived from the analysis of images that are extracted from video recordings of the dissolution process.

It is observed that silica dissolved with the average fastest dissolution time, and it was faster than the alumina and MA spinel particle; but the alumina particle dissolved significantly slower with a more uniformly linear dissolution profile.

Table of Contents

Foreword	i
Abstract	ii
List of figures and tables	v
List of figures	v
List of tables	vii
List of abbreviations and symbols	vii
Chapter 1: Introduction	9
1.1 Environmental aspects of steel production.....	9
1.2 Oxide particle dissolution.....	10
Chapter 2: Modelling of oxide particle dissolution	13
2.1 Types of modelling approach	13
2.2 Modelling approach in this work	14
2.3 Experiments with respect to oxide particle dissolution	18
Chapter 3: Dissolution experiments and observation.....	21
3.1 Materials selection	21
3.2 Experimental setup	21
3.3 Experimental steps.....	23
3.4 Calibration of sample temperature measurements.....	23
3.5 Evaluation of dissolution data	25
Chapter 4: Conclusion.....	44
Appendix.....	45
Bibliography.....	50

List of figures and tables

List of figures

Figure 1: The numerical model is represented in one dimension	14
Figure 2: An illustration of the components of the high-temperature confocal laser scanning confocal microscopy (HT-CLSM). [58]	19
Figure 3: Sketch of the HT-CLSM setup.	22
Figure 4: The CLSM high-temperature furnace. The Pt-crucible was loaded with pre-melted slag and eventually an oxide particle was dropped into this liquid.	23
Figure 5 (a-c): The plots of the three obtained reference temperatures of the sample and furnace.	24
Figure 6 (a)-(d): Dissolution of the synthetic alumina (Al_2O_3) particle in the experimental slag where the images were taken, at 381, 668, 1140 and 1447 s.	25
Figure 7: The calculated area of a dissolving spherical silica particle in SLAG 3.	27
Figure 8: Dissolution profile of the MA Spinel particle in SLAG 2.	28
Figure 9: A plot showing the characteristic dissolution time for MA spinel in Slag 1.	29
Figure 10: Dissolution profile of the alumina (Al_2O_3) particle in slag sample 1.	30
Figure 11: Evolution of gas bubbles during the dissolution of MA spinel in SLAG 1.	31
Figure 12: The dissolution profile of MA Spinel in Slag 1.	32
Figure 13: The dissolution profile of alumina in SLAG 2.....	33
Figure 14: The dissolution profile of MA spinel in SLAG 2.....	34
Figure 15: The dissolution profile of silica in SLAG 2.....	34
Figure 16: The dissolution profile of alumina in SLAG 3.....	35
Figure 17: The dissolution profile of MA spinel in Slag 3.....	36
Figure 18: The dissolution profile of silica in SLAG 3.....	37
Figure 19: Mean particle diameter D_M versus dissolution time for alumina particles in (a) slag 1 (b) slag 2 and c) slag 3.	40
Figure 20: Mean particle diameter D_M versus dissolution time for MA spinel particles in (a) slag 1 (b) slag 2 and c) slag 3.	42

List of tables

Table 1: Composition of the slag samples.....	21
Table 2. Material data sheet of the oxide particles.....	21
Table 3. Experimental data obtained from the calibration run.....	25
Table 4. The experimental particle-oxide combination.....	34
Table 5. Diffusion Coefficient Matrix for the dissolution of alumina in the samples of the CaO- Al ₂ O ₃ -SiO ₂ system	38
Table 6. Diffusion Coefficient Matrix for the dissolution of MA spinel in the samples of the CaO- Al ₂ O ₃ -SiO ₂ system	40

List of abbreviations and symbols

B_{slag}	General basicity index for slags
B_V	V-ratio
B_{MC}	Basicity index for slags with varying compositions
G	Gibbs energy
G^o	Free energy of the components
G_{mix}^{ideal}	Contribution of the ideal configuration entropy to the Gibbs energy
G_{mix}^{excess}	Difference in Gibbs energy of the real solution from an ideal solution
$G_{mix}^{physical}$	Gibbs energy contribution of physical phenomena
D	Particle's coefficient of diffusion
k	Component
x_k	Mole fraction of the diffusing component
r	Spatial coordinate
t	Time
$x_{k,i}, x_{k,i-1},$ and $x_{k,i+1}$	Different mole fractions of components in the liquid
i	Different node points
$x_{k,n+1}$	Time derivative of the mole fraction
j_k	Diffusive flux
x_k^{SOLID}	Mole fraction of the component at the solid side of the interface.
MQM	Modified quasi-chemical model
X_{A-B}	Pair bond molar fraction.
α	Molar non-configurational entropy
N	Avogadro's number
Z	Coordination number
σ	Pair non-configurational entropy
HT- CSLM	High-Temperature Laser Scanning Confocal Microscopy

Chapter 1: Introduction

“Science walks forward on two feet, namely theory, and experiment... but continuous progress is only made by the use of both.”

– Robert A. Millikan

1.1. ENVIRONMENTAL ASPECTS OF STEEL PRODUCTION

The steel industry has undergone a technological revolution in the last century, and they provide a wide spectrum of slag as one of the by-products based on different steelmaking routes. Traditionally, the steel industry depends on fossil fuels (e.g., coal) for about 75% of its energy needs. Furthermore, the steel industry is responsible for 7% of the industrially emitted Carbon dioxide [1]. The International Energy Agency (IEA) announced that the steel industry is responsible for approximately 1/5 of industrial energy, and the CO₂ emissions were estimated to increase by 30% by 2050. The output of some countries will further increase by 400% despite the global CO₂ reduction targets [2].

Grand View Research, Inc. gave a forecast that the global steel demand is expected to reach USD 1.01×10^{12} by 2025 and register a Compound Annual Growth Rate (CAGR) of 2.6%. Though China's steel production was estimated to increase in 2020 and survived the scare due to early stock build-up, there was an estimated 5% decline in global crude steel output in 2020 when compared to 2019. The industry is projected to rise from the global slump, and this is due to rising demand from players in the energy, automotive, and transportation sector over that period, aside from the anticipated rapid rise of urbanization in the emerging regions [3].

Today, there is increased government focus on the initiation and enforcement of policies that influence energy efficiency, a shift to renewable energy, material substitution, efficiency and demand reduction, and more economically attractive methods to reduce carbon emissions [4,5]. Due to the impact of these variables, worldwide iron and steel production grew rapidly during the last century from 192.03×10^9 kg in 1950 to 1908.13×10^9 kg in 2020 and there was a steep increase in the last two decades. Most of the top slag producers are in the Eurasian region from China, India, to Russia, excluding the United States [6,7].

The steel industry is currently embracing the transition energy campaign via a shift in energy generation and usage due to the current campaign for transition to zero usage of fossil fuels and venting of greenhouse gases (GHGs) to meet the target of the 2015 United Nations Climate Change Conference which has set global climate targets by 2030 in the following areas:

- a 40% reduction in greenhouse gas emissions from 1990's levels,
- a 32.5% improvement in energy efficiency in different areas of the building and industrial sector e.g., energy-efficient buildings, co-generation of heat and power, Eco-design, financing, and
- a 32% share for renewable energy and it includes biomass, hydrogen, and hydropower.

Alongside the production of steel and iron, there was a corresponding increase in slag production, its major less valuable by-product (when compared to iron and steel). The generated slags' chemical composition and their quantity depend on the choice of steel-making process and the raw materials utilized. These factors influence its classification and are as follows:

- A. Blast Furnace/Iron slags are part of the by-products obtained from the blast furnace. They are utilized for pig iron production.
- B. Steelmaking slags refer to the range of slags produced by the processes for steel production and their main constituents are calcium oxide, iron oxide, silicon oxide, and magnesium oxide. Generally, they have a higher percentage of Calcium and Silicon when compared to Iron slags. There are different classes of steel slags, and they include:
 - Electric arc furnace (EAF) slag is produced in the electric arc furnace.
 - Basic oxygen furnace (BOF) slag is created in the oxygen converter.
 - Secondary metallurgy slags are obtained from the production of special steels e.g., in ladle furnaces (LF), and
 - Stainless steel slags are by-products of the production of stainless steel in EAF, during argon oxygen decarburization (AOD), or in vacuum oxygen decarburization (VOD) furnaces.

Forming a slag with suitable properties during the steelmaking process is important for improving steel cleanliness and the process's productivity. The metallurgical slag acts as a sink for impurities, reduces thermal losses via the insulation of the liquid bath, influences the redox potential of the steel bath during refining, protects the liquid steel from re-oxidation, and prevents the entry of gases (i.e., nitrogen and hydrogen) from the atmosphere into the bath. To fulfil these various requirements the slag must have optimum physical (low melting point, low viscosity, low surface tension, and high diffusivity), thermodynamic and chemical properties (basicity, oxygen potential) [8,9].

Slag engineering is a process in steelmaking that operates on the principle of the creation of a balanced mixture of the refractory oxides (e.g., CaO and MgO) and fluxing oxides to form a suitable slag. The solid oxides from the refractory material and the fluxing oxides dissolve in the liquid slag during the steel-making process. The composition and properties of the liquid slag are thus heavily influenced by this process. A clear understanding of the dissolution of oxide particles in liquid slags is, therefore, a prerequisite to optimising slag properties according to the needs of an optimal steelmaking process.

In this work, the dissolution behavior of various oxides is investigated experimentally and from a modelling perspective.

1.2. **OXIDE PARTICLE DISSOLUTION**

Dissolution of solid oxides in slag melts occurs via two possible pathways, i.e., via a direct or, alternatively, an indirect mechanism. In direct dissolution, atoms from the solid dissolve directly into the melt without the formation of an intermediate solid reaction product [10]. Indirect dissolution defines a process in which an intermediate solid product forms at the solid/liquid interface during the dissolution of the oxide particle in the liquid slag. While a fast and direct dissolution mechanism is favourable in terms of a rapid dissolution of fluxing agents, slow, indirect dissolution may be favourable to extend the service life of the refractory lining by protecting the refractory materials [13,14].

According to the well-known shrinking core model the dissolution kinetics may be dictated by the chemical reaction resulting in the formation of a new phase, diffusion through the reaction product, diffusion in the bulk material, or a combination of several kinetic steps [11,12]. It is of vast importance to identify those critical kinetic steps to understand and properly describe the dissolution of solid oxides in metallurgical slags.

The dissolution process of an oxide particle in molten slag is heavily influenced by the constitution of the liquid phase.

Oxides form ionic complexes in the melt they might act as acidic network formers (e.g., Al_2O_3 , SiO_2 and P_2O_5) or basic network modifiers (e.g., CaO , MgO , FeO_x). The ratio of the concentrations of basic oxides to those of the acidic oxides is defined as the slag's basicity [15,16].

Slag basicity is regularly expressed in several ways which are shown below.

- The most common definition of basicity is called the V ratio and is shown below in equation (3).

$$B_{slag} = \frac{\sum(\%basic\ oxide)}{\sum\%acidic\ oxide} \dots\dots\dots (1)$$

$$B_V = \frac{wt\%CaO}{wt\%SiO_2} \dots\dots\dots (2)$$

where B_{slag} is the general basicity index for slags, B_V is the V-ratio, wt%CaO and wt%SiO₂ are the weight percentage of CaO, and SiO₂ [15]. Slags are considered basic only when the CaO content is higher than 66.7wt%. Slag basicity is divided into low (0.93 -1.4), medium (1.4 - 1.87), high (1.87-2.80) and multi-basic (≥ 2.80).

In a multi-component slag with different basic oxides, it may be favourable to express the basicity in a differently by considering the effect of MgO and Al_2O_3 on the properties of the slag:

$$B_{MC} = \frac{\%CaO + \%MgO}{\%SiO_2 + \%Al_2O_3} \dots\dots\dots (3)$$

here, B_{MC} is the basicity index for slags with varying compositions [17].

The constitution of slag can be easily classified via the basicity index. It is a valuable reference for the selection of refractory material used in a metallurgical process. Basic refractories for instance can never be used in combination with acidic slags as they would rapidly dissolve in the slag and eventually lose their function. However, the basicity alone may not be a sufficient characteristic for predicting the influence of the slag composition on the dissolution behaviour of oxide particles in liquid slags. A more sophisticated approach is the use of thermodynamic models.

Thermodynamic models are important in the design of processes and operating practices without a priori experimental data and provide additional insights into the dissolution process that are missing in the experiments because the volume of generated data points is limited, sporadic and averaged over time [18].

A fundamental step in a thermodynamic analysis of a process is calculating the equilibrium conditions at given conditions. When the system is having constant pressure and temperature, the Gibbs energy (G) is the potential to be reduced to find the equilibrium conditions of a thermodynamic system. It is shown below in equations (4) and (5).

$$G = G^o + G_{mix}^{ideal} + G_{mix}^{excess} + G_{mix}^{physical} \dots \dots \dots (4)$$

Where G is the Gibbs energy, G^o is the free energy of the components, G_{mix}^{ideal} is the contribution of the ideal configuration entropy to the Gibbs energy, G_{mix}^{excess} is the difference in Gibbs energy of the real solution from an ideal solution, and $G_{mix}^{physical}$ denotes the Gibbs energy contribution of physical phenomena (e.g. magnetic effects).

Chapter 2: Modelling of oxide particle dissolution.

2.1 TYPES OF MODELLING APPROACHES

Identifying the rate determining kinetic steps is a major task in predicting the dissolution behaviour of oxide particles in metallurgical slags. To enhance the understanding of dissolution processes relevant for steelmaking, several modelling approaches have been undertaken in various studies. A selection of well-established modelling approaches is introduced in the following.

2.1.1 LATTICE BOLTZMANN METHOD

It operates on the premise that simple arithmetic calculations can be used to simulate complex fluid flows without solving complicated partial differential flow equations [19-21]. The fluid flow is treated as mean populations which are a set of distribution functions or artificial particles (which is a function of location, time, and microscopic velocity), and operates based on their collision.

The hydrodynamic variables are expressed at each lattice point in terms of a distribution function, unlike the conventional numerical schemes that rely on the discretization of macroscopic continuum equations. This feature is advantageous when studying non-equilibrium dynamics, especially in fluid applications that involves interfacial phases and complicated boundaries geometries with less computational cost [22-37].

Verhaeghe et al. [38] used the numerical tool of Lattice-Boltzmann modelling (LBM) and verified it with CSLM dissolution experimental data to determine the dissolution mechanism of Al_2O_3 in CAS slags between 1470 to 1550 °C. It is assumed that the dissolving oxide particles are stationary, and the dissolution process is diffusion controlled.

The rate-limiting step was determined by comparing the results of the numerical simulations to the experimental data. All the experimental temperatures, the simulation results fitted the experimental dissolution curves better than the SCM model [39].

2.1.2 PHASE FIELD MODELLING

Phase-field modelling is based on the idea that interfaces in microstructure are diffuse at the nanoscale and can be represented by one or more smoothly varying order parameters [39-43].

The phase field method is used in the visualisation of evolution of microstructure without having to track the movement of individual interfaces. It eliminates the need to explicitly track interfaces, which would require defining boundary conditions and deriving evolution equations for each interface [43].

Aside from the total free energy (G) of the volume, the phase field method has several components, and they are as follows:

- The order parameter: a single variable that represent the state of the microstructure

- The width of the interface: the range over which the order parameter changes from one phase to another

Some advantages of the PFM approach include:

- i. It is well suited for the visualisation of microstructural development.
- ii. The number of particles in the system is much greater than the number of equations to be solved.

It is a flexible method to model various phenomena e.g., morphology changes and overlap of diffusion fields. PFM has some issues, so the quantitative modelling of experimentally relevant situations is not always possible [39-44]. There are several severe disadvantages, and they are as follows:

- i. Its application is limited to recalculating experimentally observed evolving morphology.
- ii. The interface width may be set to physically unrealistic values [43].

That is why the predictive power of this method has its limitations.

2.2 MODELLING APPROACH IN THIS WORK

The numerical modelling approach used in this work is based on the work of Ogris and Gamsjäger [45]. The following assumptions are made:

- i. The system is one-dimensional with a spherical boundary
- ii. Two phases are present in the system, and they include the solid phase (oxide particle) and the liquid phase
- iii. A sharp (i.e., infinitely thin) interface exists between the phases.
- iv. An equilibrium exists at the interface between both phases.
- v. The interfacial tension along the particle-liquid interface is uniform.
- vi. Diffusion occurs only in the liquid phase
- vii. The diffusion coefficient of the solid particle is not constant in varying liquid oxide melt.
- viii. The overall dissolution rate is influenced by the diffusion of cations through the interface.

The diffusion equation for the spherical geometry is followed as:

$$\frac{dx_k}{dt} = D \left(\frac{d^2 x_k}{dr^2} + \frac{2}{r} \frac{dx_k}{dr} \right) \dots \dots \dots (5)$$

where D is the particle's coefficient of diffusion, x_k is the mole fraction of the diffusing component k , r is the spatial coordinate and it ranges from the particle's radius to system's outer boundary, and t is time. The partial differential equation is integrated numerically via a central approximation finite-difference scheme.

The Fick's second law is discretized and transformed via the finite difference approximation. It is shown below.

$$\frac{\Delta x_k}{\Delta t} = D \left(\frac{\Delta x_{k,i-1} + \Delta x_{k,i+1} - 2x_{k,i}}{\Delta r^2} + \frac{2}{r_i} \frac{x_{k,i+1} - x_{k,i-1}}{2\Delta r} \right) \dots \dots \dots (6)$$

Where, $x_{k,i}$, $x_{k,i-1}$, and $x_{k,i+1}$ are different mole fractions of components k in the liquid at different time steps, and i represent the different node points.

The rate of change of the mole fraction with time can be represented in a numerical model as shown below in Figure 1. The node points range from $n+1$ to $p-1$ where p is the system boundary vertex. A local equilibrium exist at the interface whose position is represented as n , and the fluxes j_k are all zero at the system boundary which is represented by the nodal point p .

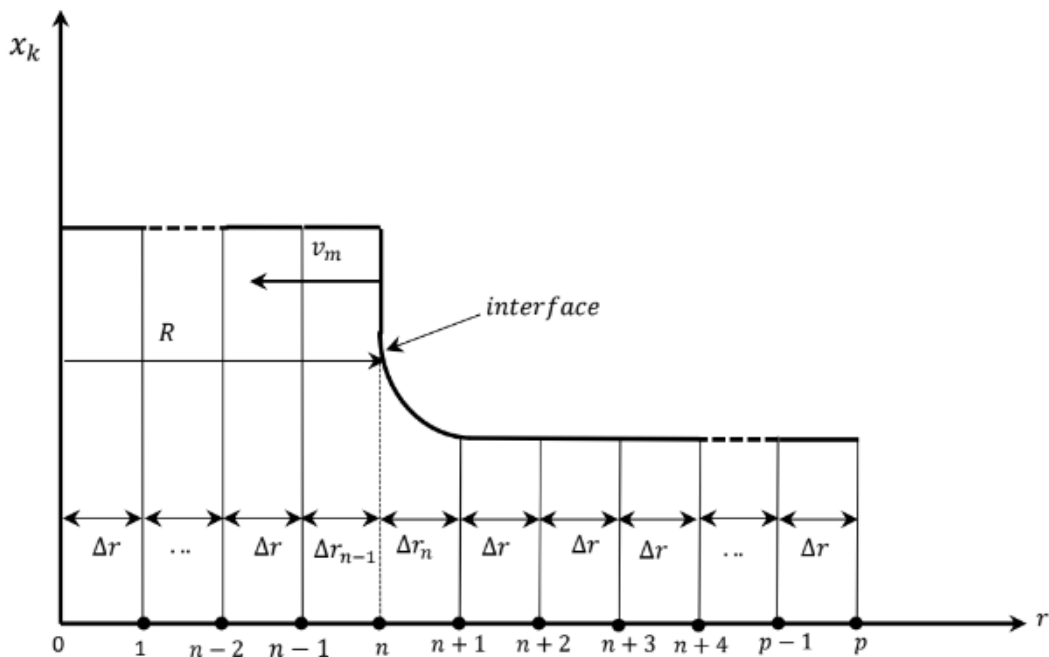


Figure 1. The numerical model is represented in one dimension.

At node $n+1$, the mole fractions is solved as a parabola ($x_k = ar^2 + br + c$), and its coefficients a , b and c are shown below in equations (7) to (9).

$$a = \frac{x_{k,n}\Delta r + x_{k,n+2}\Delta r_n - x_{k,n+1}(\Delta r + \Delta r_n)}{\Delta r_n \Delta r (\Delta r_n + \Delta r)} \dots \dots \dots (7)$$

$$b = \frac{x_{k,n+2}\Delta r_n^2 - x_{k,n}\Delta r^2 + x_{k,n+1}(\Delta r^2 + \Delta r_n^2)}{\Delta r_n \Delta r (\Delta r_n + \Delta r)} \dots \dots \dots (8)$$

$$c = x_{k,n+1} \dots \dots \dots (9)$$

A combination of equations (7) and (8) will result in the mole fraction's time derivative when it is inserted into the diffusion equation as shown in equation (10), and it is shown below.

$$x_{k,n+1} = 2aD \left(3 + \frac{b}{ar_{n+1}} \right) \dots \dots \dots (10)$$

Where $x_{k,n+1}$ is the time derivative of the mole fraction.

The diffusive flux j_k of the components k at the interface n of the solid-liquid melt is calculated using:

$$j_{k,n} = \frac{\frac{\Delta r + \Delta r_n}{2} r_{n+1}^2 x_{k,n+1} + \sum_{i=n+2}^p \Delta r r_i^2 x_{k,i}}{V_m \left(r_n + \frac{\Delta r_n}{2} \right)^2} \dots \dots \dots (11)$$

Where the index n represent the interface, components is k , the system's boundary, vertex is p , molar volume is V_m , the time is t , the spatial coordinate is r , and R is the radius of the solid particle.

Finally, the interface velocity v is calculated.

$$v = \frac{j_n V_m}{(x_k^{SOLID} - x_{k,n})} \dots \dots \dots (12)$$

Where x_k^{SOLID} is the mole fraction of the component k at the solid side of the interface.

The mobility of the interface does not interfere with the movement of the interface as its mobility is infinitely high in this model. This is a direct consequence of the local equilibrium assumption at the interface. The calculation of the local equilibrium at the interface is undertaken using a Gibbs energy minimization routine, see [42]. The thermodynamic properties of the liquid slag are calculated using the modified quasi-chemical model as introduced by Pelton et al. [46-48].

The modified quasi-chemical model (MQM) considers strong SRO effects between constituents of a phase. Short-range-ordering (SRO) refers to local ordering phenomena on distances close to the atomic spacings due to configurations of atomic pairs.

In the MQM for binary solutions, the particles A and B are distributed substitutionally on the site of a quasi-lattice where their nearest neighbours can be a pair of like or unlike particles (namely, AA, AB, BB pairs). The relative amounts of pairs are determined by the energy change associated with the formation of two AB pairs from an AA and BB pair [46]. In an oxide melt, the second - nearest-neighbour (SNN) pair exchange reaction between the ionic species A and B is shown below in Equation (13).



Where $(A - B)$ represents the nearest neighbour pair and Δg_{AB} represents the Gibbs free energy change forming two moles of $(A - B)$ pairs, and its sign and magnitude determine if this formation of $(A - B)$ pairs is thermodynamically favourable.

- When Δg_{AB} is negative and high, it signifies the presence of an ordered solution (i.e., (AB) pairs are favourable).

- If Δg_{AB} becomes positive, it shows the occurrence of the immiscible solution signifying the clustering of (AA) and (BB) pairs.
- If $\Delta g_{AB} = 0$, the solution becomes an ideal mixture.

Denoting the number of moles of species A and B by n_A and n_B , and the number of moles of $(A - B)$ pairs by n_{AB} , the following mass balance in Equations (14) and (15) are obtained:

$$Z_A n_A = 2n_{AA} + n_{AB} \dots \dots \dots (14)$$

$$Z_B n_B = 2n_{BB} + n_{AB} \dots \dots \dots (15)$$

Where the parameters, Z_A and Z_B represent the coordination numbers (i.e., the total number of the particle's neighbours) of species A and B . The factor 2 represent the two i particles that form the n_{AB} pair.

The mole fraction X_A and coordination fraction Y_A of particle A , and the pairs defined by:

$$X_A = \frac{n_A}{n_A + n_B} = 1 - X_B \dots \dots \dots (16)$$

$$Y_A = \frac{Z_A n_A}{Z_A n_A + Z_B n_B} = \frac{Z_A X_A}{Z_A X_A + Z_B X_B} = 1 - Y_B \dots \dots \dots (17)$$

The pair fraction X_{ij} is given by:

$$X_{ij} = \frac{n_{ij}}{n_{AA} + n_{BB} + n_{AB}} \dots \dots \dots (18)$$

Equation (18) can be modified as shown below.

$$X_{ij} = \frac{2n_{ij}}{Z_A n_A + Z_B n_B} \dots \dots \dots (19)$$

The Gibbs energy of mixing, ($\Delta G'$) at a given temperature (T) is computed and shown below.

$$\Delta G' = \frac{n_{AB}}{2} \Delta g_{AB} - T \Delta S^{mix} + (g_A^0 n_A + g_B^0 n_B) \dots \dots \dots (20)$$

Where n_A and n_B is the number of moles in the atoms of components A and B , the factor 0.5 occurs as Δg_{AB} is the Gibbs free energy resulting from the formation of two $(A - B)$ pairs, g_A^0 and g_B^0 are the molar Gibbs energies of the pure components A and B , and ΔS^{mix} is the configurational entropy of mixing given by a random distribution of the pairs in the one-dimensional Ising approximation.

$$\Delta S^{config} = -R(n_A \ln X_A + n_B \ln X_B) - R [n_{AA} \ln \left(\frac{X_{AA}}{Y_A^2} \right) + n_{BB} \ln \left(\frac{X_{BB}}{Y_B^2} \right) + n_{AB} \ln \left(\frac{X_{AB}}{2Y_A Y_B} \right) \dots \dots \dots (21)$$

where n_x represents the numbers of moles of each pair (AA, BB, and AB).

Molar enthalpy change could be written as:

$$\omega = \frac{N*Z}{2} (2\varepsilon_{A-B} - \varepsilon_{A-A} - \varepsilon_{B-B}) \dots \dots \dots (22)$$

Where ω is the molar enthalpy change, N is the Avogadro's number, Z is the coordination number, and ε is the pair bonding energy. Also, the molar non-configurational entropy change could be written as:

$$\alpha = \frac{N*Z}{2} (2\sigma_{A-B} - \sigma_{A-A} - \sigma_{B-B}) \dots \dots \dots (23)$$

where α is the molar non-configurational entropy, N is the Avogadro's number, Z is the coordination number and σ is the pair non-configurational entropy. The mixing enthalpy and non-configurational entropy can then be calculated as:

$$\Delta H_{MIX} = (X_{A-B} * 0.5)\omega \dots \dots \dots (24)$$

$$\Delta S^{nonconfig} = (X_{A-B} * 0.5)\mu \dots \dots \dots (25)$$

Where X_{A-B} is the pair bond molar fraction.

The total entropy change (S^E) upon forming solution also contains the configurational entropy term which is:

$$\Delta S^{config} = -R(X_A \ln X_A + X_B \ln X_B) - 0.5RZ \left(\frac{X_{A-A} \ln X_{A-A} + (X_{B-B} \ln X_{B-B})}{X_A^2} \right) + \left(\frac{X_{B-B} \ln X_{B-B}}{X_B^2} \right) + \left(\frac{X_{A-B} \ln X_{A-B}}{2X_A X_B} \right) \dots \dots \dots (26)$$

The equilibrium constant for the quasi-chemical reaction is given below:

$$\frac{X_{AB}^2}{X_{AA}X_{BB}} = 4e^{\frac{-2(\omega_{AB}-\mu T)}{zRT}} \dots \dots \dots (27)$$

When the model parameter (Δg_{AB}) becomes more negative, there is an increase in the formation of (A – B) pair, and the reaction moves to the right [45].

The modified quasi-chemical equations can be extended to ternary and multicomponent systems.

2.3 EXPERIMENTS WITH RESPECT TO OXIDE PARTICLE DISSOLUTION

There are different experimental techniques used to study the mechanism of lime dissolution in slags and they may involve in-situ experiments or ex situ experiments which utilize characterization tools for post-mortem examination, (e.g., microstructure determination and composition analysis).

Dynamic tests are carried out by sampling from an industry converter and by forced convection where it is carried out by eccentrically stirring the molten slag (containing a lime cube), stirring slag with the aid of an impeller, and/or argon gas bubbling in slag via an iron tube.

The most common technique used for the investigation of the dissolution mechanism is the finger test technique where a rotating or static solid oxide (e.g., lime) cylinder is dipped into molten slag and after a period of exposure, the cylinder is removed and characterized. An analysis of the distribution of the phases across the cylinder, gives the dissolution kinetics and mechanisms [49-53].

However, this method suffers as:

- I. Ex situ determination,
- II. Dissolution kinetics is influenced by the rotation rate. This is due to the movement of the lime cylinder which is relative to the slag, and it is being refreshed with slag free of the reaction products.
- III. Damage of the cylinder can affect the analysis of the phases.
- IV. There is a rapid saturation of the slag composition with reaction products.

Static tests are carried out by the iteration of the reaction over different times, temperatures and, slag chemistry while holding the slag in a dense lime crucible, or by varying temperature, while a piece of lime is reacting with slag in the crucible.

Direct observation is a form of static test which includes the in-situ observation of dissolution of lime particle in slag with the aid of X-ray radiography and High Temperature Laser Scanning Confocal Microscopy (HT-CLSM) observation [54-58].

In 1961, Minski established the principles of laser scanning confocal microscopy (CSLM) [55], but it was in the 1990s that Emi and co-workers [54] combined CSLM with infrared heating to carry out real-time investigation of crystal growth and transformations in Fe–C alloys.

A High-Temperature Laser Scanning Confocal Microscopy (HT- CSLM) system is made up of an infrared image furnace (IIF), a collimated laser beam, and confocal optics. It is mainly employed for the in-situ observation, control, recording and analysis of the oxide dissolution process at high temperatures [57]. It is also used in several experimental studies to observe other metallurgical phenomena which including phase transformations of metallic alloys, oxidation and reduction

processes, the morphology of solidification, inclusion behaviour in slags, the crystallisation behaviour of slags, and kinetics of peritectic transformations.

A schematic sketch of the High-Temperature Laser Scanning Confocal Microscopy (HT-CLSM) set-up is shown below in Figure 2.

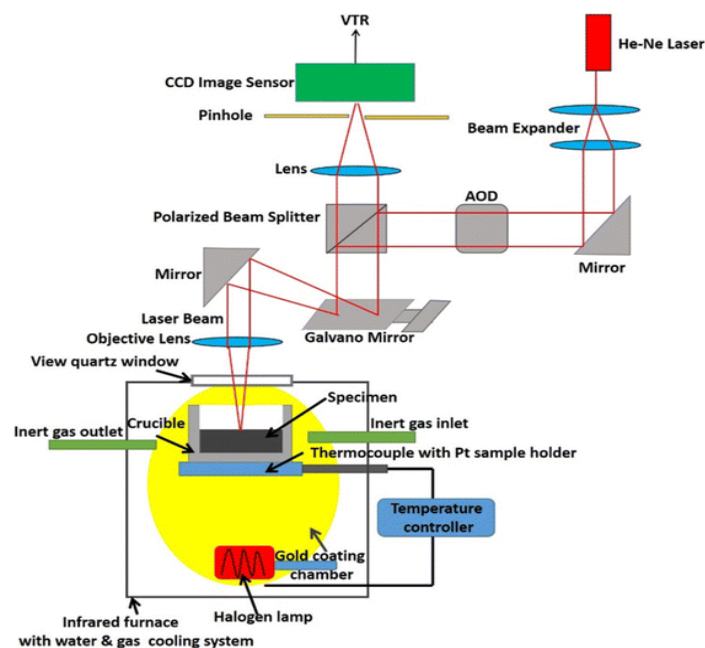


Figure 2: An illustration of the components of the high-temperature confocal laser scanning confocal microscopy (HT-CLSM) [58].

Some of the characteristics and advantages of High-Temperature Laser Scanning Confocal Microscopy are as follows [56-58]:

- Moving image observation of samples with high magnification (up to 3000x) and high contrast at high temperature.
- Sample temperatures can be controlled between -100 and 1800 degrees Celsius.
- The possibility of the visualization of fine surface asperities.
- Experiments can be conducted in a vacuum or using a defined furnace atmosphere.
- No chemical etching is required as thermal etching renders that process.
- The entire process is caught on video (up to 10-hour video recording and replaying).

CSLM has some limitations [53-58], and they are listed below.

- I. The relative density of the particle influences the particle trajectory i.e., it can lead to the flotation of the particle on the molten slag's surface (the requirement for this experiment) or sinking to the crucible's bottom.
- II. The heating rate should be set to ensure that particle dissolution starts at the designed temperature because the particle is likely to be dissolved before reaching the experimental temperature if it is too slow, and the furnace temperature can exceed the experimental temperature if it is too high.
- III. For easy identification of the particle-liquid interface, the particle should have relatively low porosity to inhibit the bubble formation during inclusion dissolution.
- IV. High cost of acquisition and operation of equipment
- V. When compared to the other methods, it is complicated to operate

A major advantage of this system is the versatility of experimental design which permit the use of different reaction atmospheres and a range of possible sample heating and cooling rates. It usually includes an infrared heating chamber with a cooling rate of several 100K/min. The entire process is recorded using a DIC system with a thermal imaging camera which operates at a maximum frame rate of 60 pictures per second at a temperature range between -20 °C to 1500 °C [56,58].

Chapter 3: DISSOLUTION EXPERIMENTS AND OBSERVATION

3.1 MATERIALS SELECTION

The materials used in the experiment include oxide particles (silica (SiO_2), alumina (Al_2O_3), and magnesium aluminate (MgAl_2O_4)) and varying samples of pre-melted slag that is composed of $\text{CaO-Al}_2\text{O}_3\text{-SiO}_2$. The selected particles are spherical with an initial diameter D ($D = 500 \pm 25 \mu\text{m}$). Three slag samples, labelled 1, 2 and 3 were prepared, where each sample is characterized by its amount of CaO , Al_2O_3 and SiO_2 . The slags are liquid for the temperatures and compositions used in these experiments. They are listed in Table 1.

Table 1: Composition of the slag samples

SLAG	COMPOSITION BY WEIGHT PERCENTAGE		
	CaO	Al_2O_3	SiO_2
1	25	15	60
2	35	20	45
3	30	17.5	52.5

Physical properties of the selected oxide particles (Sandoz precision spheres) are presented in Table 2 and originate from data sheets of the manufacturer of the particles (Sandoz Fils SA, Switzerland).

Table 2: Material data sheet of the oxide particles. [59]

	PARTICLE	SIZE	DENSITY
1	Alumina (Al_2O_3)	0.20 to 150mm	3.96 g/cm^3
2	Spinel ($\text{MgO}\cdot\text{Al}_2\text{O}_3$)	0.20 to 8.00mm	3.61 g/cm^3
3	Fused silica (SiO_2)	0.30 to 25.40mm	2.20 g/cm^3

3.2 EXPERIMENTAL SETUP

A Lasertec VL2000DX Digital Confocal Scanning Laser Microscope (CSLM) with a high-temperature furnace type SVF17-SP (Yonekura), and a programable temperature controller were used for the in-situ observations. A sketch of the CSLM apparatus is presented in Figure 3. Experiments with the CSLM included: The pre-melting of the synthetic slag and the dissolution of the oxide particles in the transparent slags at high temperature.

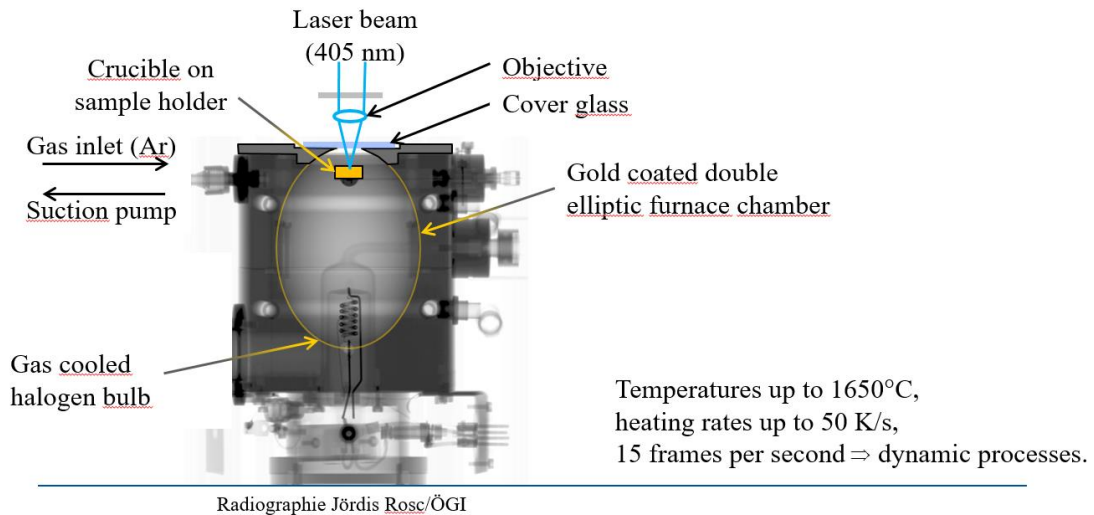


Figure 3: Sketch of the HT-CLSM setup.

The setup has several parts which include cooling inlets (air and water), a cooling outlet (air), a gold-coated ellipsoidal furnace, a sample holder, a 1.0 kW halogen lamp, and a lamp bulb protection tube. The process takes place inside a gold-plated chamber where a halogen bulb is in the lower focal point and the sample is in the upper focal point. This arrangement allows the reflection of infrared radiation produced from the bulb to be focused on the sample and to heat the sample.

The sample stage consists of a protruding rod so that the sample can be positioned in the centre of the second focal point). The R-type thermocouple is spot-welded to the sample holder at the end of the rod. Wires inside the hollow rod connect this thermocouple to the measuring device (see Figure 4).

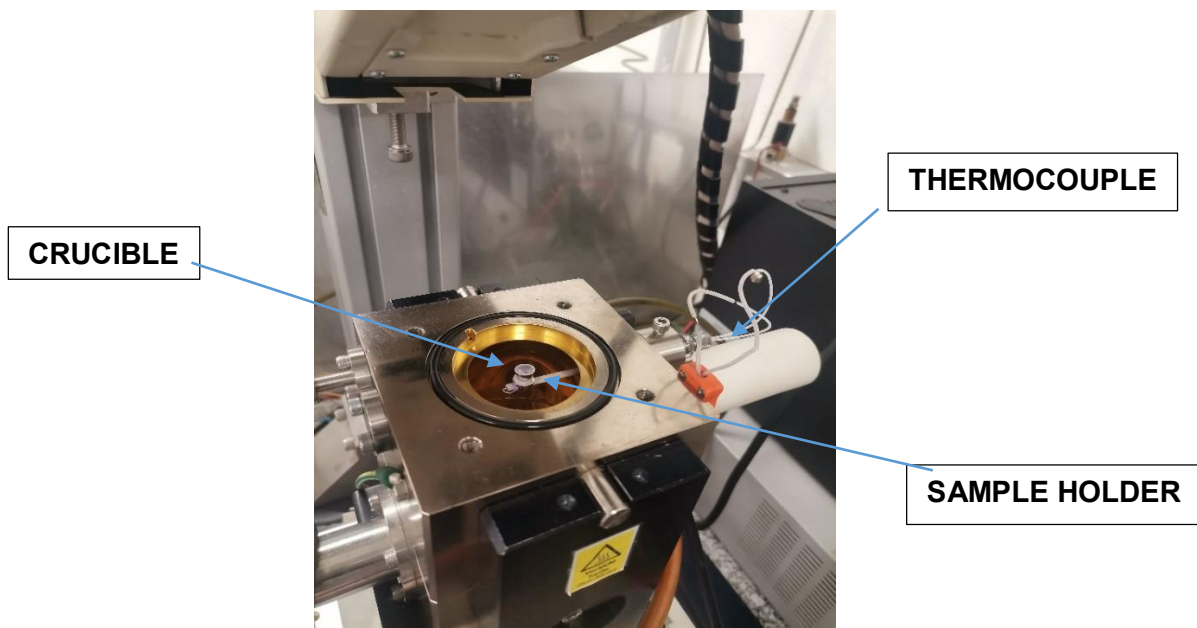


Figure 4: The CLSM high-temperature furnace. The Pt-crucible was loaded with pre-melted slag and eventually an oxide particle was dropped into this liquid.

3.3 EXPERIMENTAL STEPS

The experimental steps for the dissolution experiment are as follows:

- I. The slag was first prepared by mixing the selected compounds. The mixture was then melted in a furnace at 1600°C.
- II. A sample was collected, ground, and filled into a platinum crucible.
- III. The slag was pre-melted in the heating chamber of the HT-CSLM by its placement in a platinum crucible which is on a sample holder, and it can be observed.
- IV. The particle was placed in the pre-melted slag and the experiment was started.
- V. The temperature increased until the target experimental temperature was reached with a constant Ar-flow.
- VI. The dissolution process was recorded and stored in video format.

3.4 CALIBRATION OF SAMPLE TEMPERATURE MEASUREMENTS

The system was calibrated for temperature to obtain an accurate temperature of the slag melt in the HT-CSLM. This is because the direct measurement of the slag temperature is not possible. S-type thermocouples were used for temperature measurement and provided feedback to the halogen lamp power supply controller. They are welded to the sample holder of the HT-CSLM. The experimental target temperature must be calibrated with a slag sample with similar properties (known melting point in the temperature range that range from room temperature to about 1550°C).

The temperature difference between the thermocouple that was dipped into the slag (control thermocouple) and the thermocouple that was welded to the sample holder of the HT-CSLM is recorded. The temperature of the furnace and the derived temperature of the sample are plotted versus time in Figs 8 a-c. The real temperature of the slag in the isothermal tests is derived from this experiment.

A series of calibration runs were conducted before the dissolution experiments began. The temperature reading is obtained from the thermocouples attached to the furnace and the sample holder but there is an observed inconsistency between them, hence a calibration process has to be done in order to get a reading that is error free. The results obtained is used to calibrate the temperature reading obtained during the dissolution experiments.

In Figure 5 below, a reference measurement is required to obtain the accurate slag temperature. The calibration procedure had to be repeated for each series of experiments. The calibration curves (furnace temperature (T_F / °C) and sample temperature (T_S / °C) versus time (t/s)) for an experimental run I is presented in Fig. 5a, for an experimental run II in Fig 5b; and for an experimental run III in Fig. 5c.

Table 3 show the relevant experimental data from the calibration runs when regression analysis was carried out. The fitted or estimated simple linear regression mode, y , is given in the table. Also, the plots produced the degree of fit parameter (R^2) plots, and the obtained values were in the range between 0.97 and 1 which indicated that within the margin of error, the plots were progressively linear with time.

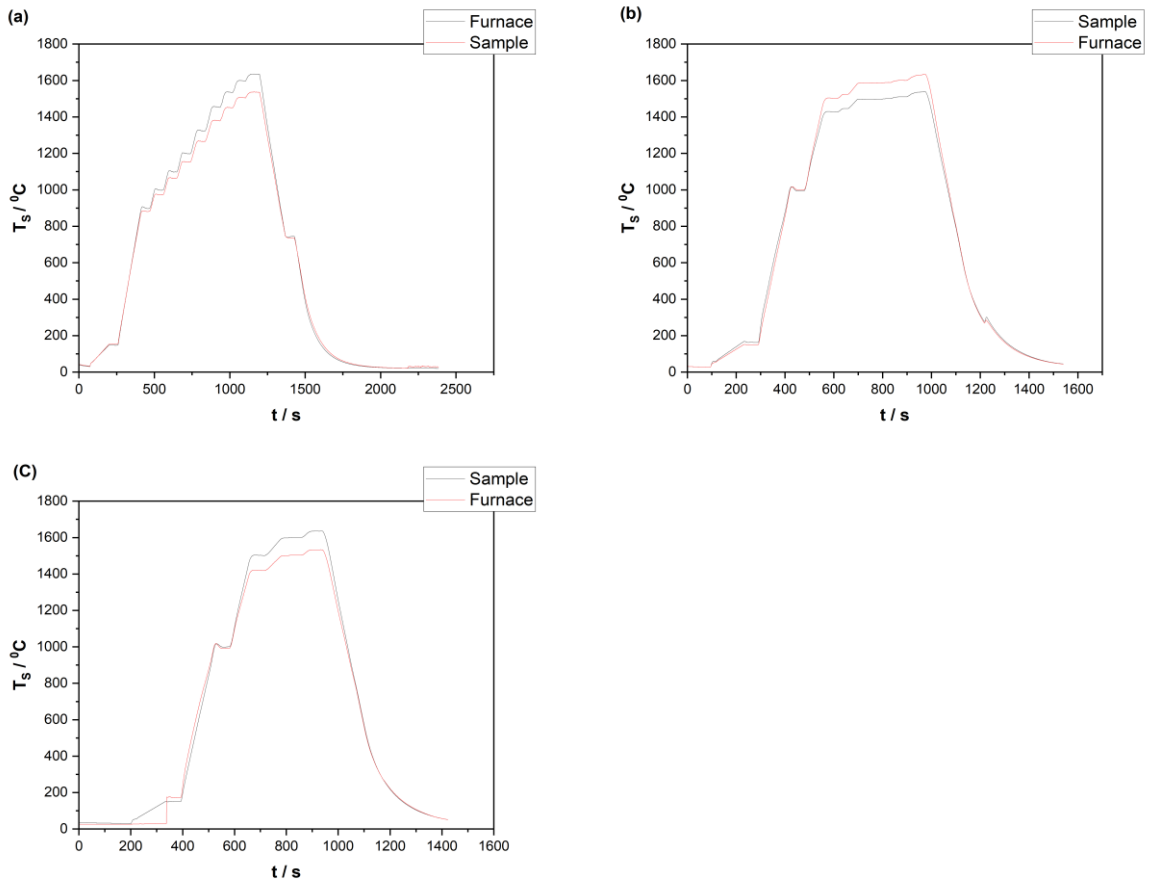


Figure 5 (a-c): The plots of the three obtained reference temperatures of the sample and furnace.

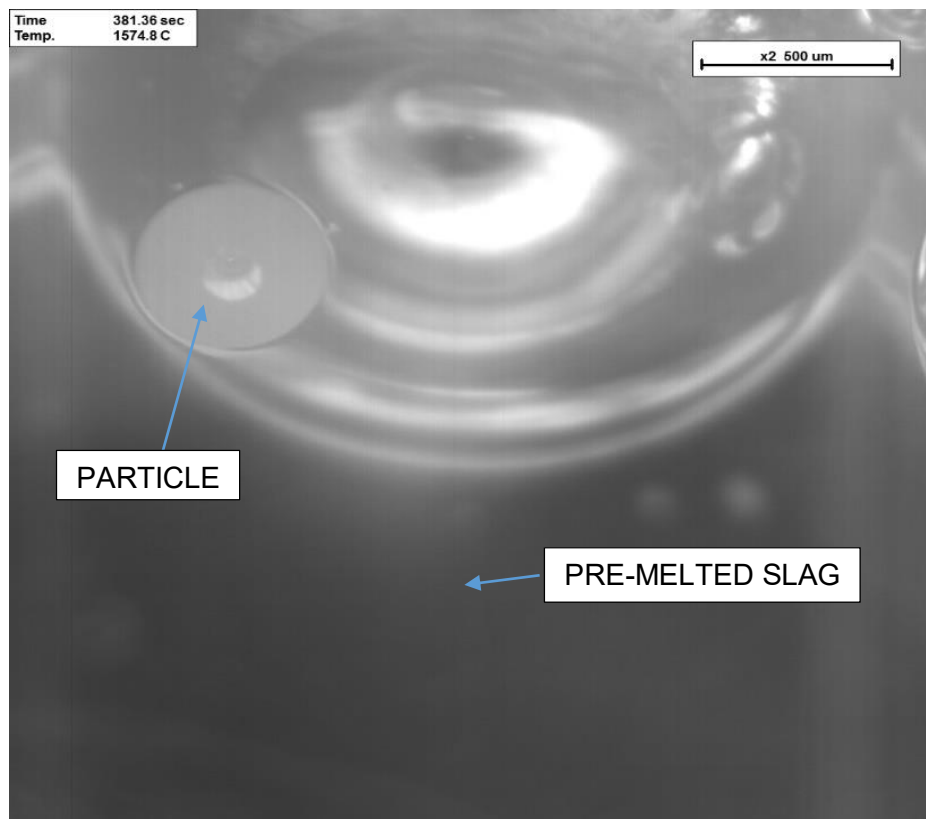
Table 3: Experimental data obtained from the calibration run

REFERENCE	SAMPLE	EXPERIMENT NUMBER	EQUATION
1	SLAG 1	3	$y = 0.95 \pm 0.019$
	SLAG 1	5	$y = 0.95 \pm 0.019$
	SLAG 2	11	$y = 0.95 \pm 0.019$
	SLAG 2	14	$y = 0.95 \pm 0.019$
	SLAG 2	17	$y = 0.95 \pm 0.019$
2	SLAG 3	21	$y = 0.84 \pm 0.0015$
3	SLAG 3	24	$y = 0.98 \pm 0.004$
	SLAG 3	26	$y = 0.98 \pm 0.004$

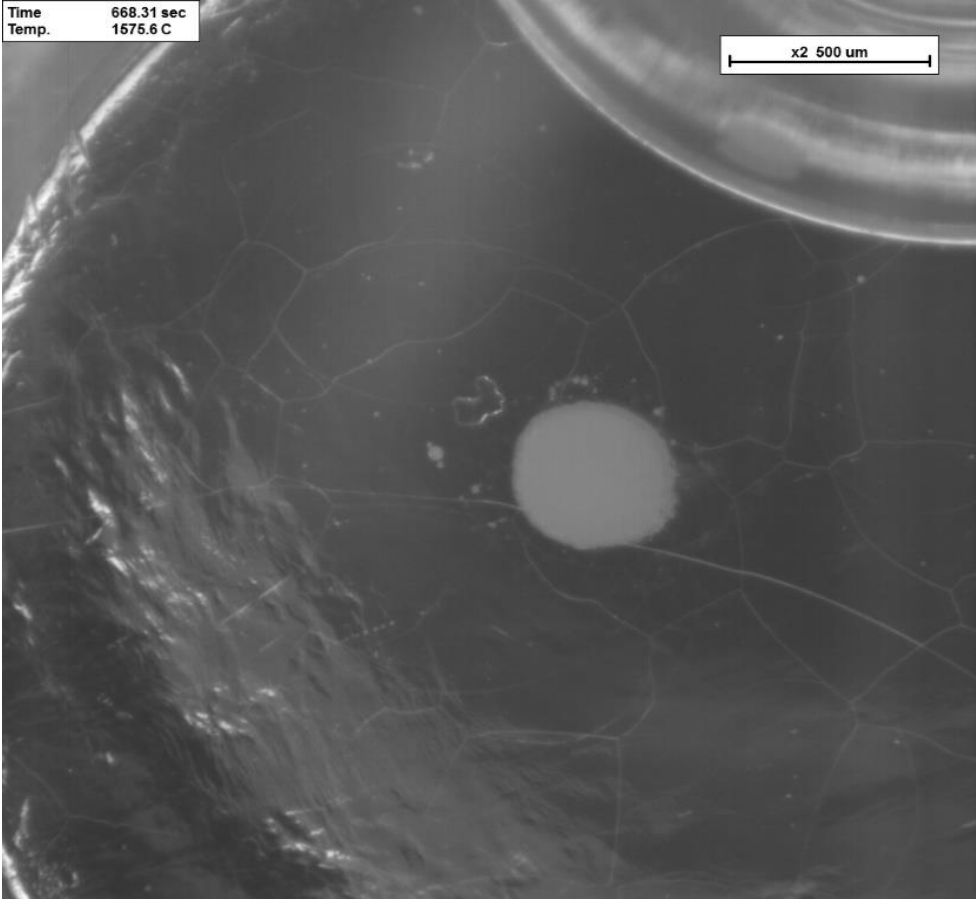
3.5 EVALUATION OF DISSOLUTION DATA

The images of the experiment were captured on a charge-coupled device (CCD) (e.g., camera), projected on a computer monitor, and obtained from the video recording component of the HT- CSLM. The dissolution kinetics of the particle is monitored during isothermal holding. Frames are extracted from the videos via VirtualDub [60].

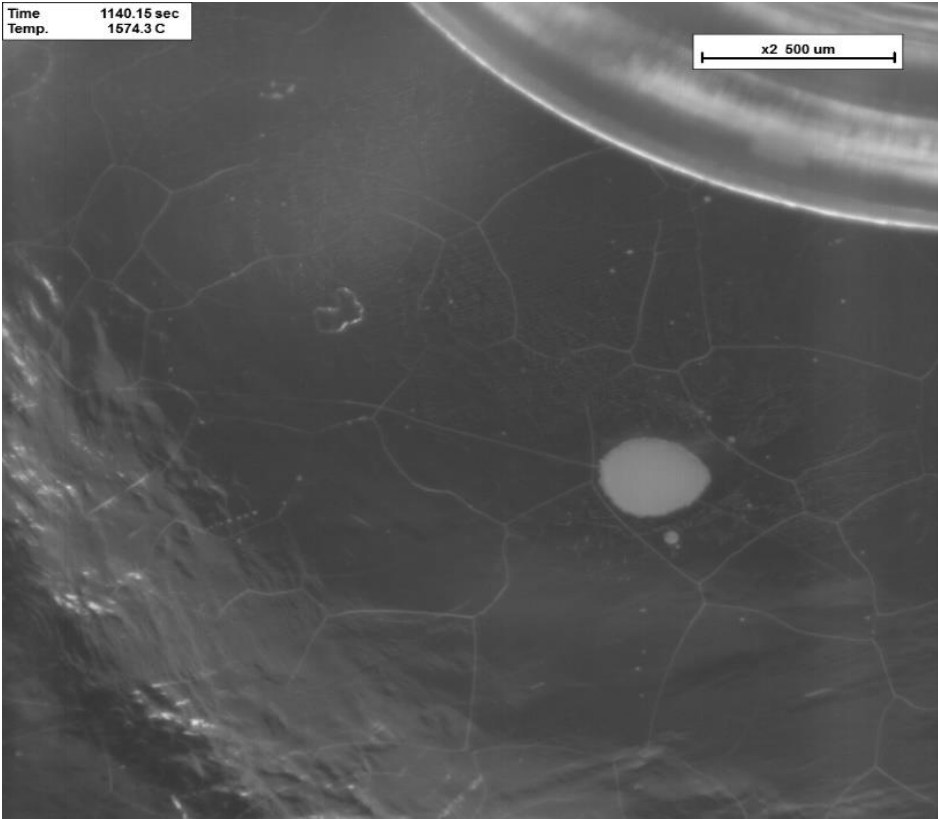
The sequence of captured images (Figures 6a-d) was obtained from the dissolution of an alumina (Al_2O_3) particle in SLAG 1 where uniform dissolution was observed and there was little or no rotation of the particle as the dissolution took place at recorded time intervals in the crucible which carried the transparent oxide pre-melt. The edge of the crucible is visible in Figure 6b. The image sequence usually ended when the oxide particle was almost completely dissolved in the slag and, thus, not anymore present in the next frame.



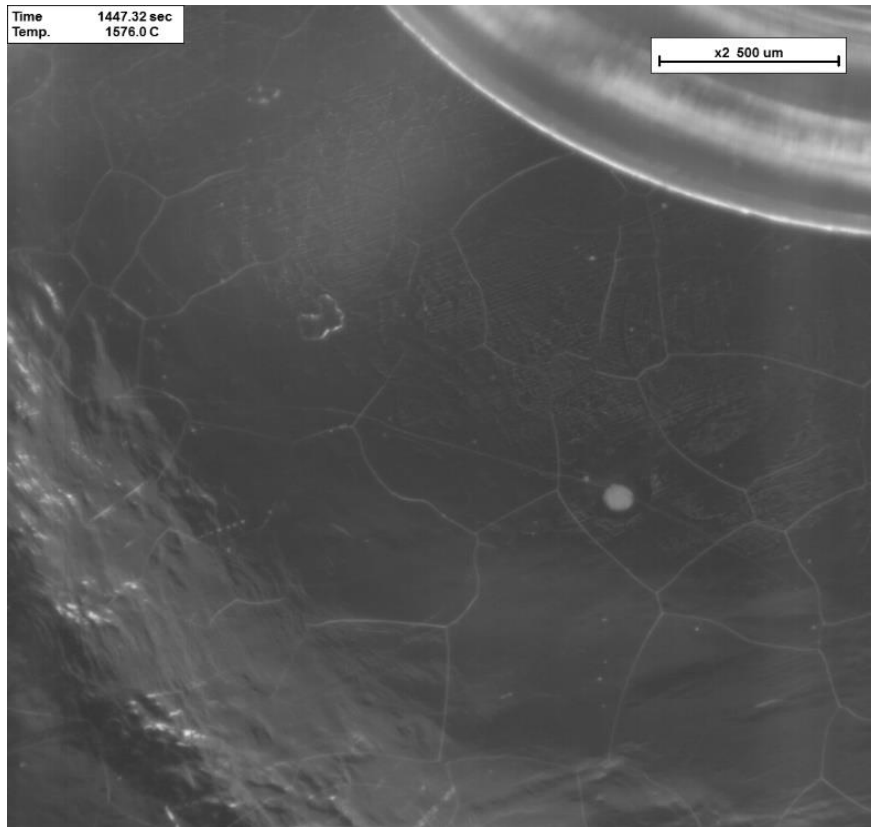
(a)



(b)



(c)



(d)

Figure 6 (a)-(d): Dissolution of the synthetic alumina (Al_2O_3) particle in the experimental slag where the images were taken, at 381, 668, 1140 and 1447 s.

Several frames (up to 100 frames) have been extracted from the recorded video of the dissolution and then the images were analysed with the software “Jens Rüdigs Makroaufmaßprogramm” [61]. This involved several steps which included the selection and definition of the image scale ($500\mu\text{m}$), and the tracing of the particles’ perimeter with the aid of a computer mouse. The area of the traced particles is computed automatically.

This can be seen below in the image shown in Figure 7, and it was obtained from the analysis of an image obtained from the video recording of the dissolution of the silica particle in $\text{CaO-Al}_2\text{O}_3\text{-SiO}_2$ (SLAG 3). The databox in the upper right region of Figure 8 depicts the scale of each extracted image and it depends on the choice of thermocouple used during the experiment. The diameter of the selected thermocouple wire was $500\mu\text{m}$. The databox in the upper left region of the image indicates the furnace temperature and the experimental time. The particle diameter is measured manually for each frame.

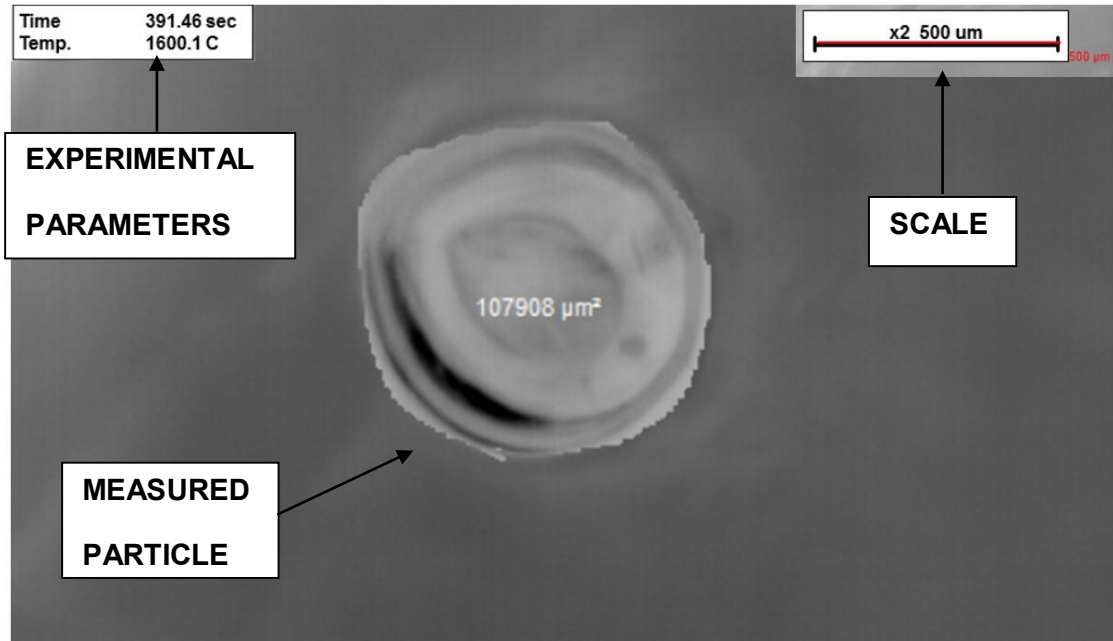


Figure 7: The calculated area of a dissolving spherical silica particle in SLAG 3.

3.5.1 EXPERIMENTAL ANALYSIS

A sequence of frames with a shrinking particle in each frame provides us then with a data set of particle diameters versus time. An exemplary resultant dissolution profile is shown below in Figure 8, where the time-dependent rate change in the particle’s diameter is shown as the green circles seen in the scatterplot. The evolution of gas bubbles during particle dissolution corrupts the unbiased detection of the particle size in some frames. This means that not all the frames can be properly analyzed.

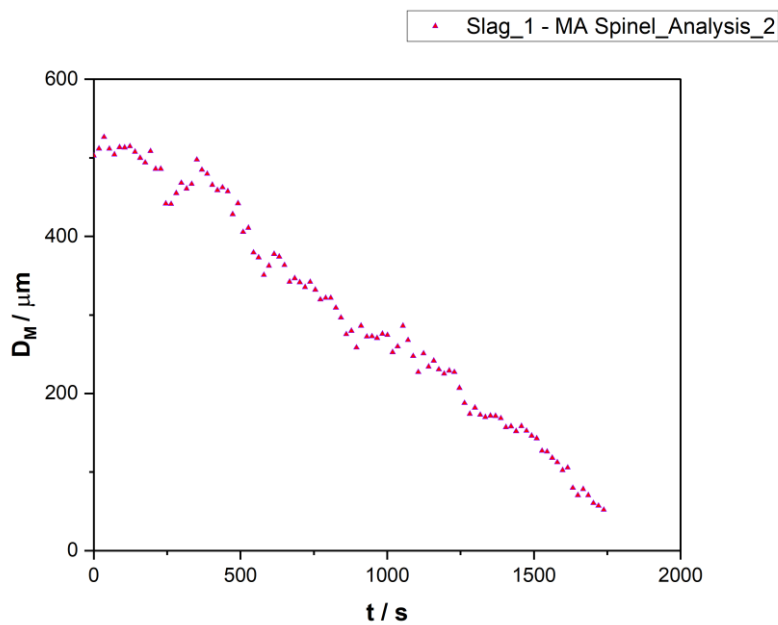


Figure 8: Dissolution profile of the MA Spinel particle in SLAG 2.

Ultimately, this is one of the sources of the scatter of the dissolution data. An additional (systematic) error is expected from the two-dimensional evaluation of the process, which is three-dimensional. It is furthermore assumed but not completely true that the initially spherical particle retains its shape until it dissolves.

A characteristic dissolution time for the dissolution experiments can be deduced from the experimental data in the following way. The time starts when there is a 10% reduction in the original diameter of the oxide particles. The characteristic dissolution time is the time that elapsed before the diameter of the particle is reduced to 90% of the initial size. Thus, experimental uncertainties during the start and at the very end of the dissolution process are avoided.

$$\Delta t = t_1 - t_2 \dots\dots\dots (28)$$

Where Δt is the estimated total dissolution time, t_1 is the time where there is a 10% decrease in the dissolving particle's diameter, and t_2 is the time at which there is a 90% reduction in the particle's diameter before the total dissolution or the end of the experiment. This is shown in shown below in Figure 10 where there is a graph of mean diameter, D_M , vs dissolution time, t . The characteristic dissolution time for MA spinel in Slag 1, as seen in Figure 9, was calculated to be 1496.6s.

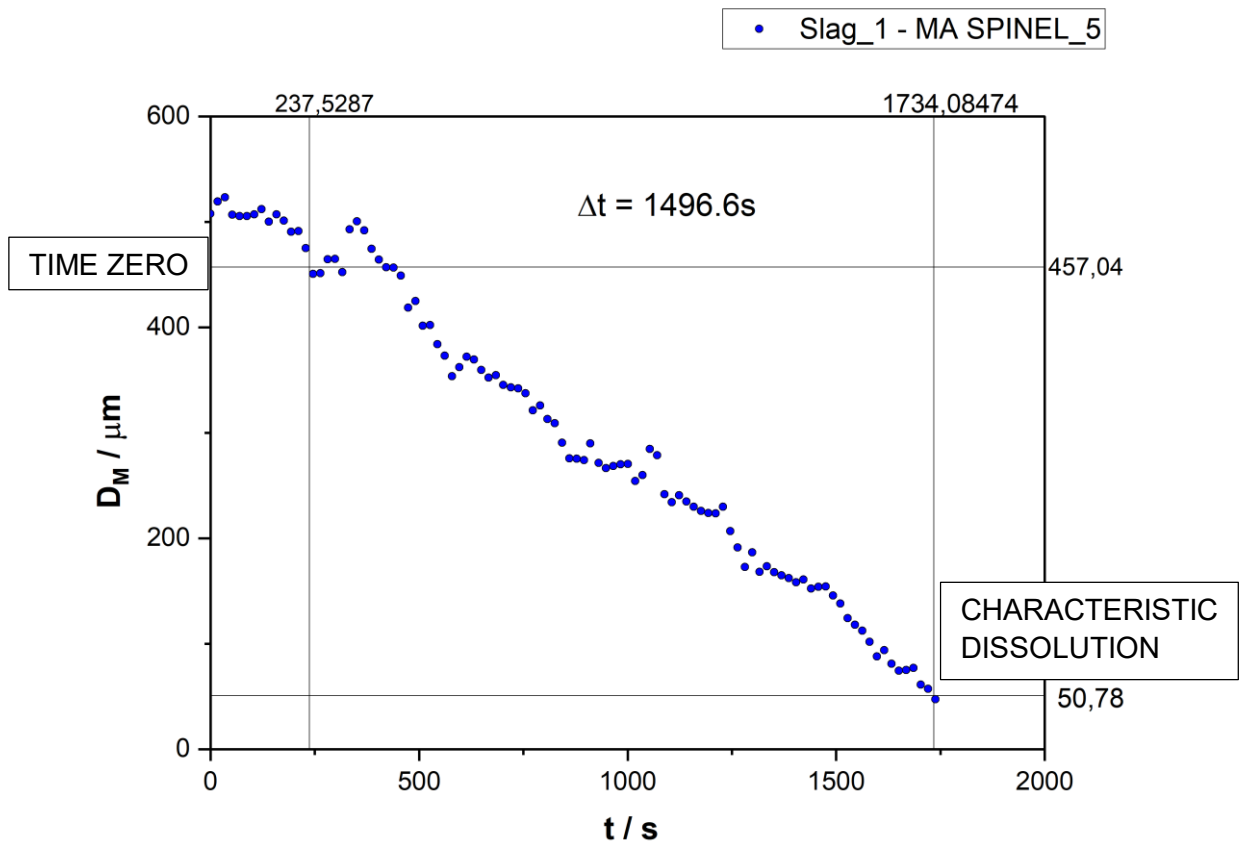


Figure 9: A plot showing the characteristic dissolution time for MA spinel in Slag 1.

The different compositions of the slags and the particles to be dissolved in these slags are summarized in Table 3. In addition, the characteristic dissolution time for the different particles in the different slag systems is presented in Table 4.

Table 4: The experimental particle-oxide combination

SLAG	COMPOSITION (CaO-Al ₂ O ₃ - SiO ₂) (Mass fraction)	OXIDE PARTICLE	CHARACTERISTIC DISSOLUTION TIME, Δt (s)	MEAN TEMPERATURE (°C)
1	0.25 - 0.15 - 0.6	Alumina	2889	1510
		MA spinel	1497	1508
		Silica	-	-
2	0.35 - 0.20 - 0.45	Alumina	2121	1509
		MA spinel	1206	1508
		Silica	452	1508
3	0.30 - 0.175 - 0.525	Alumina	608	1492
		MA spinel	871	1503
		Silica	36	1506

Three independent image analysis are carried out to improve the statistical reliability of the data that is obtained from the analysis of the image sequence (from the video recording of the change of its morphology versus time. From the three-image analysis runs the mean values and standard deviations of individual data points are calculated and used in the following analysis.

SLAG 1

The dissolution of alumina and MA spinel particles is investigated first in SLAG 1:

ALUMINA:

A distinguishable boundary was observed between the dissolving particle and the bulk pre-melted slag during the process of dissolution. Three independent image analysis were carried out to estimate the variability of the diameter measurements and to improve the accuracy of the analysis by measuring the statistical error that arises from the measurement. The mean diameter of the alumina particle during dissolution in SLAG 1 is shown in Figure 10 together with the standard deviation in the form of error bars for each value.

The characteristic dissolution time (Δt) as defined above for the alumina particle was found to be 2889.31s and is provided in Table 4.

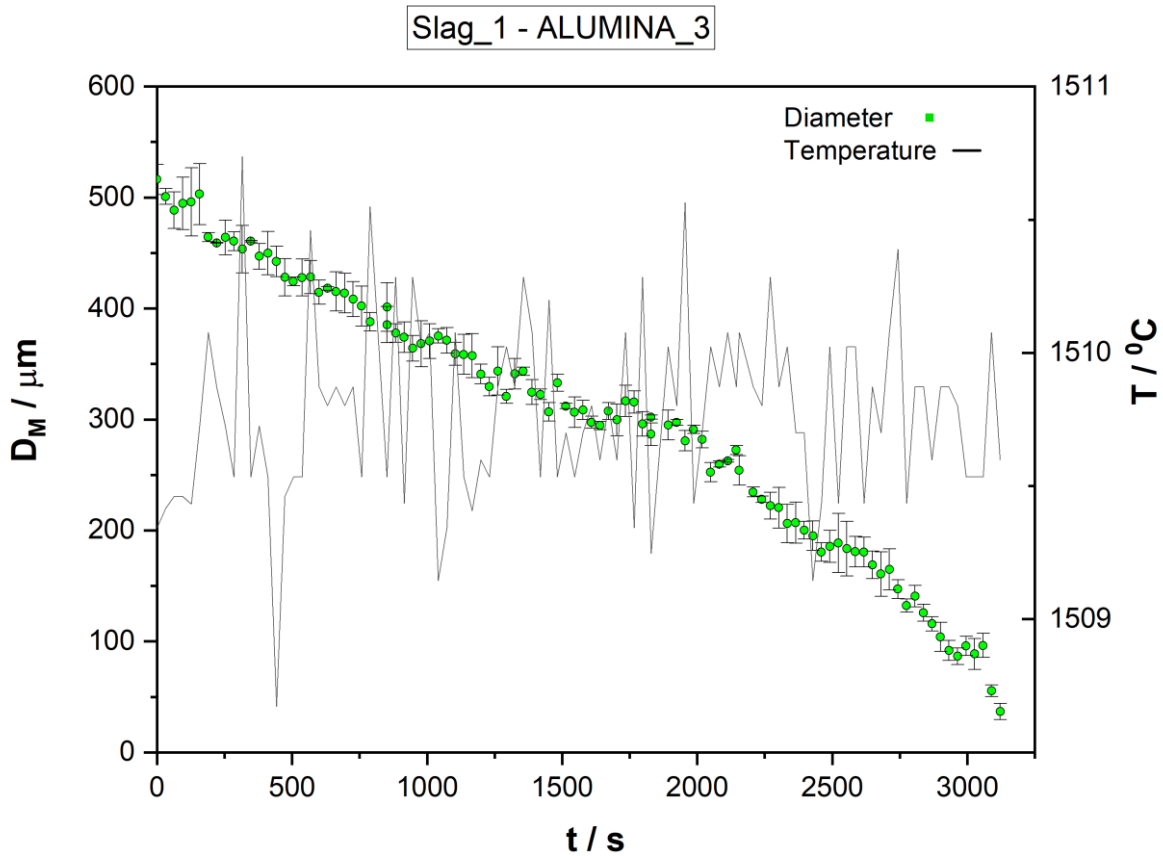


Figure 10: Dissolution profile of the alumina (Al_2O_3) particle in slag sample 1.

MA SPINEL

Small air bubbles were present during the dissolution of MA spinel in SLAG 1, as can be seen in Figure 11. The gas evolution is due to the difficulty in completely removing all entrapped gas bubbles during the pre-melting of the slag sample in the crucible. This influences the data analysis, thereby causing scatter in the dissolution profile.

In Figure 12, the mean average of the particle diameter (obtained from the three independent image analysis) was plotted against the dissolution time to give the dissolution profile. The error bars in Figure 12 represent the standard deviation for the particle diameter. This allows for roughly estimating the measuring error of the diameter of the dissolving particle. The characteristic dissolution time for MA spinel in SLAG 1 is provided in Table 4.

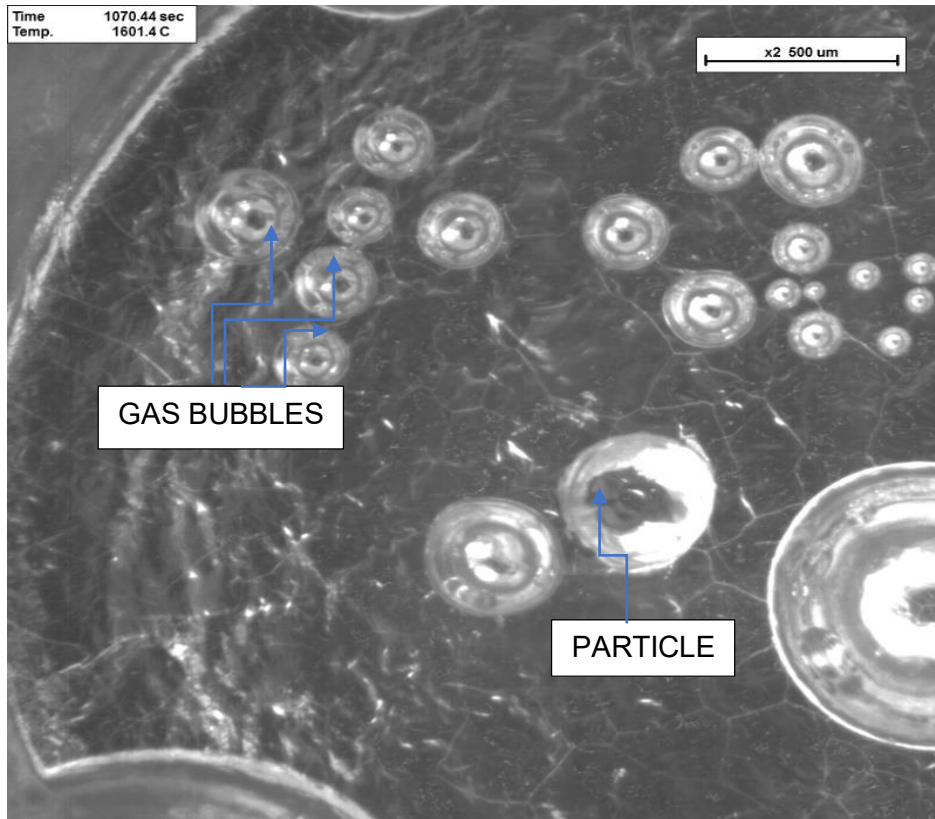


Figure 11: Evolution of gas bubbles during the dissolution of MA spinel in SLAG 1

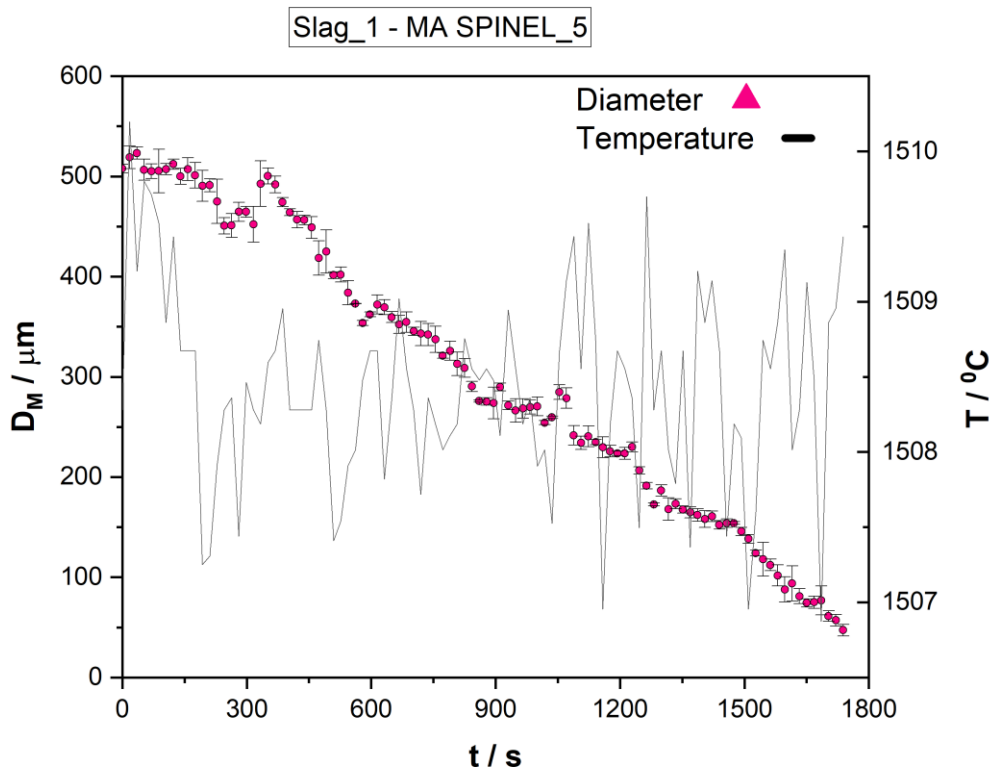


Figure 12: The dissolution profile of MA Spinel in Slag 1.

SILICA: The dissolution of the silica particle could not be analyzed effectively due to poor image quality, and this influenced the number of collected data points. It negatively affected the statistical accuracy of the analysis.

SLAG 2

SLAG 2 has a composition of (35wt%CaO - 20wt%Al₂O₃ - 45wt%SiO₂) and unlike in SLAG 1, the dissolution process of all particles (silica, alumina and MA spinel particles) could be observed. The analysis is given below.

ALUMINA: The dissolution profile of alumina in SLAG 2 is shown in Figure 13. The characteristic dissolution time (Δt) of the alumina particle was estimated to be 2120.8s and is also provided in Table 4. It appears that the dissolution of alumina in SLAG 2 is effectively faster than in SLAG 1.

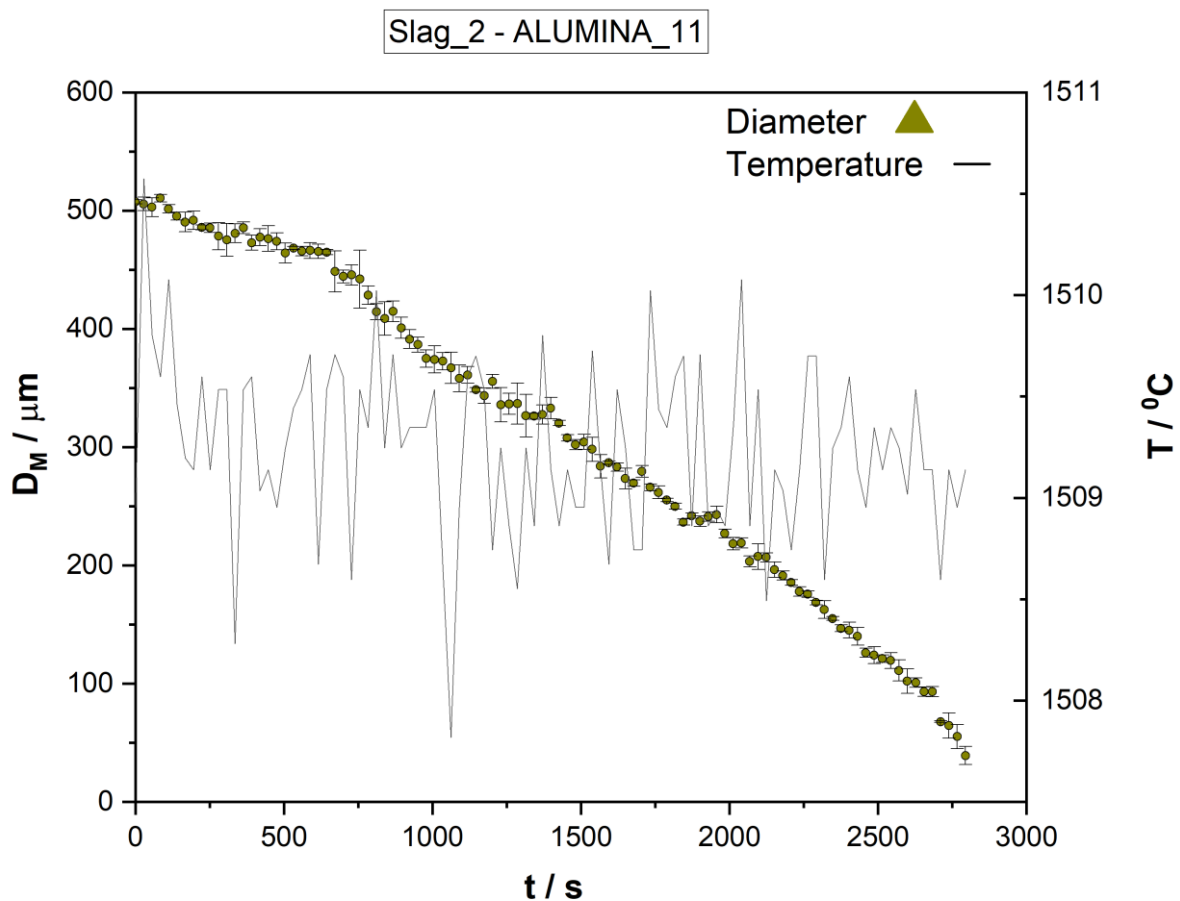


Figure 13: The dissolution profile of alumina in SLAG 2

MA SPINEL: During the dissolution of MA spinel in SLAG 2, almost no gas bubbling was observed which allowed for an undisturbed evaluation of the image sequence in this regard. The particle dissolved in SLAG 2 at an average characteristic dissolution time of 1205.74s (also see Table 4) which was faster than that of the particle in Slag 1, and the dissolution profile can be observed to be steeper (see Figure 14).

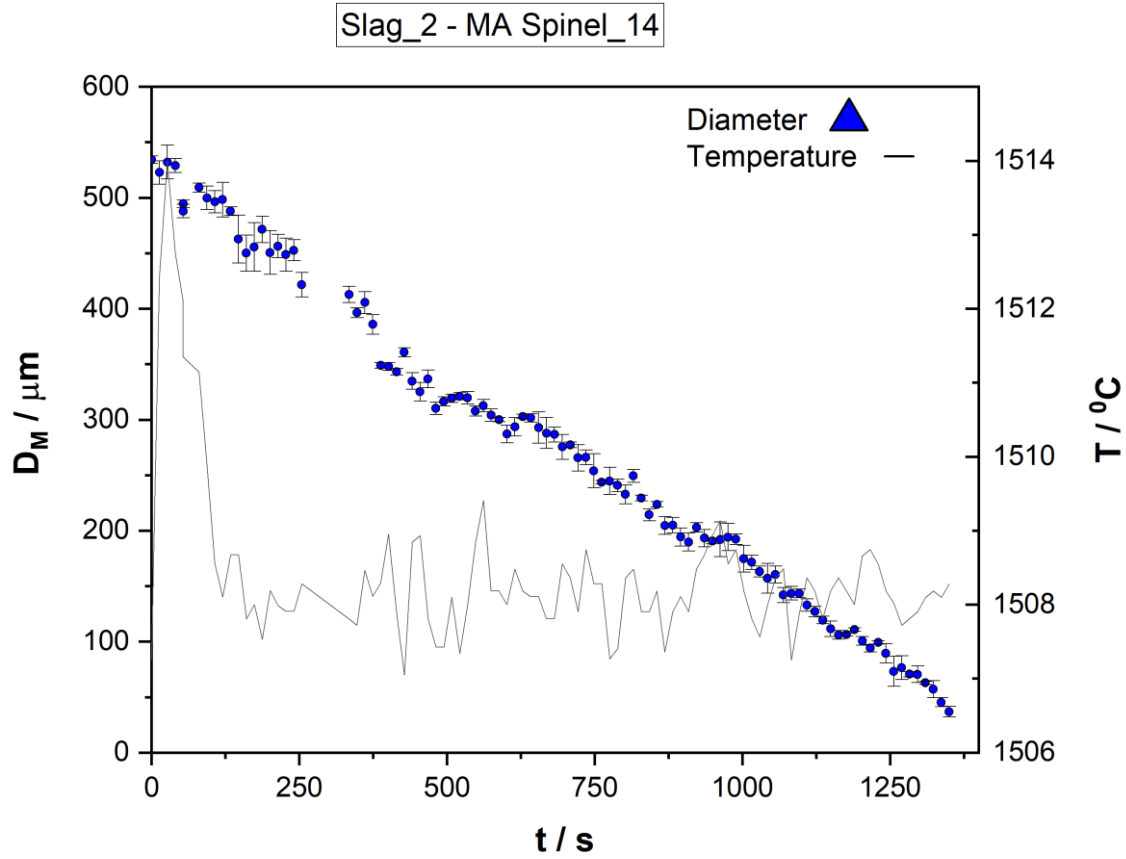


Figure 14: The dissolution profile of MA spinel in SLAG 2

SILICA: The dissolution profile for a silica particle in SLAG 2 is shown in Figure 15 together with the standard deviation calculated from three independent image analysis. The resulting dissolution profile is steep with a sharp dip when the particle reaches 250 μm , as can be seen in Figure 16. The characteristic dissolution time for silica is given in Table 4.

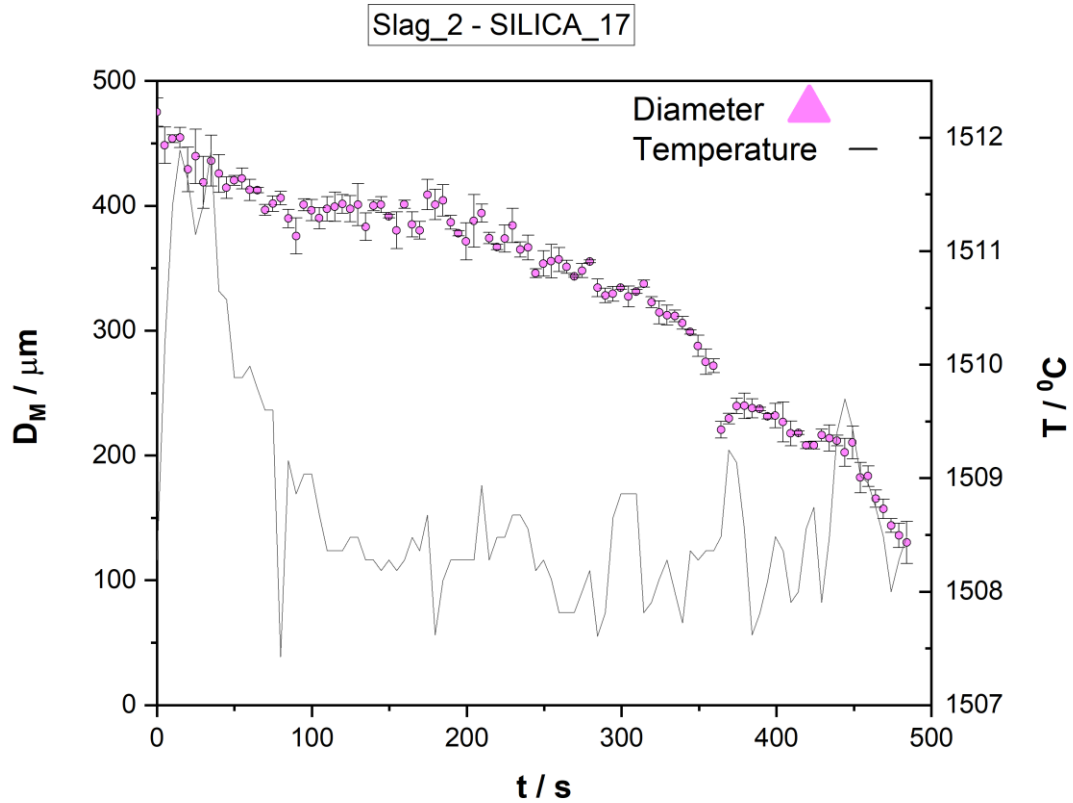


Figure 15: The dissolution profile of silica in SLAG 2

SLAG 3

SLAG 3 has a composition of CaO-Al₂O₃-SiO₂ (30%, 17.5%, 52.560%) and the analysis of the dissolution process of the alumina, silica and MA spinel particles dissolved and was analyzed.

ALUMINA: The alumina particle dissolved in the slag at an average dissolution time (Δt) of 607.7s (see also Table 4) The change in the particle morphology was uniform until it is dissolved totally. The mean diameter vs dissolution time for the alumina dissolution in SLAG 3 is shown in Figure 16. It is evident by comparing the characteristic dissolution times in Table 4 which indicates that the dissolution of alumina in SLAG 3 is slower than in SLAG 1 and SLAG 2.

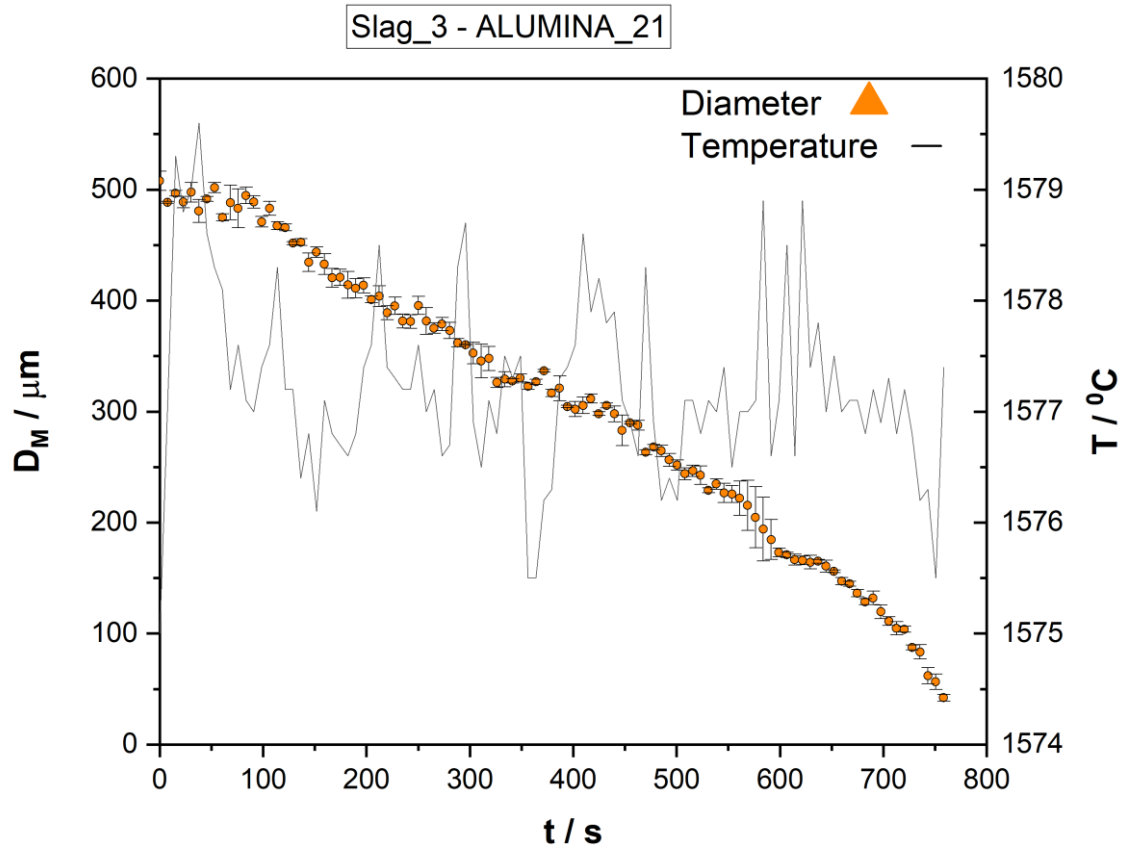


Figure 16: The dissolution profile of alumina in SLAG 3

MA SPINEL: The shape of the dissolution profile for MA spinel particle in SLAG 3 is like that of the dissolution profile of MA spinel in SLAG 1 and SLAG 2. Only little evolution of gas bubbles was observed. There was negligible or no rotation of the particle, but it was observed that it moved a lot in the oxide melt until total dissolution was achieved. The dissolution rate was linearly step as can be seen in Figure 17. The characteristic dissolution time was calculated and is given in Table 4.

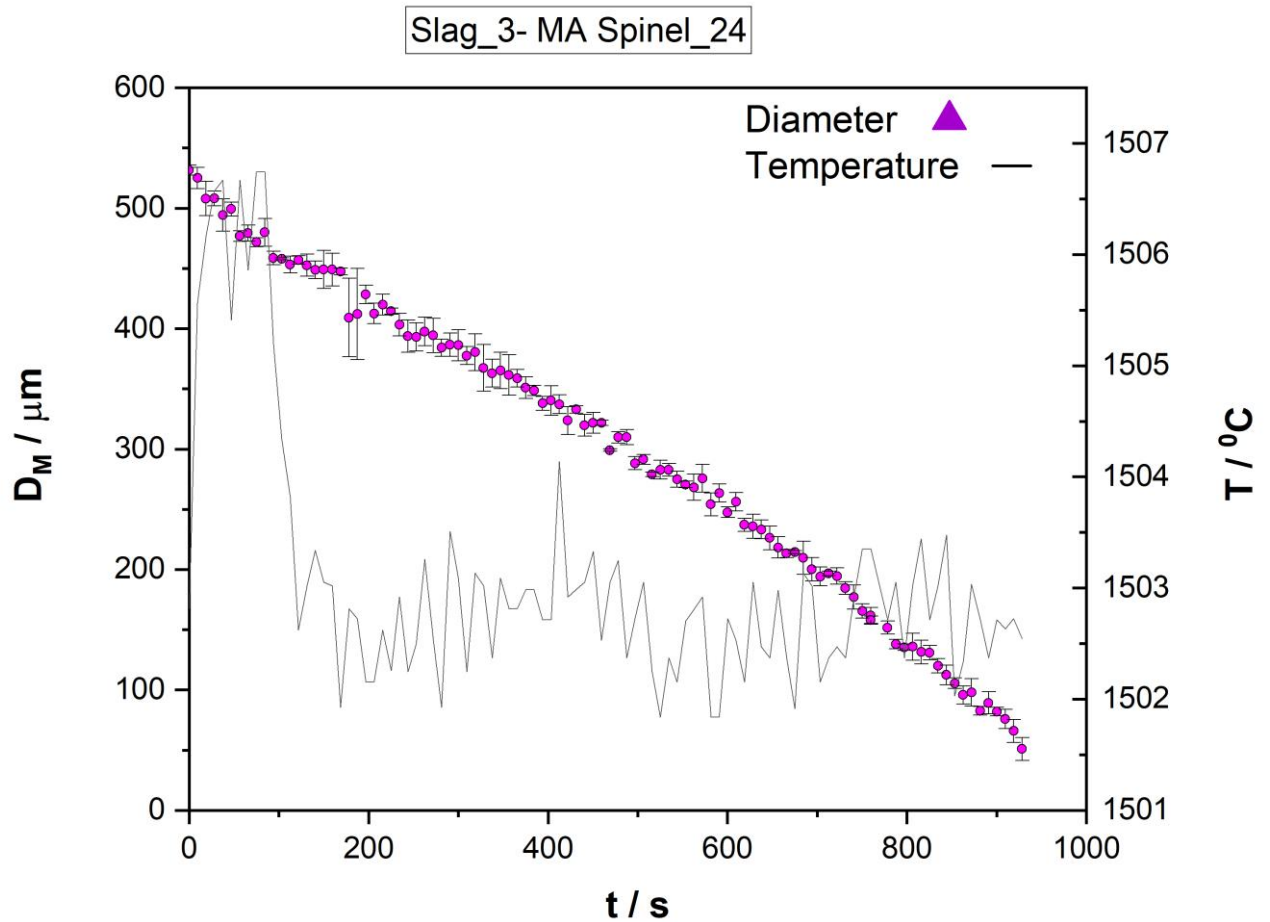


Figure 17: The dissolution profile of MA spinel in Slag 3

SILICA: It was observed that the dissolution rate of silica in SLAG 3 was very rapid. The silica particle kept its spherical shape throughout the dissolution process. The dissolution profile for silica in SLAG 3 can be seen in Figure 18. The remarkable scatter in the observed mean diameter of the silica particle during dissolution is due to the difficulty of evaluating the particle diameter clearly from the derived image sequence. Unfortunately, no higher quality measurements could be achieved in this work. The characteristic dissolution time was calculated and is provided in Table 4.

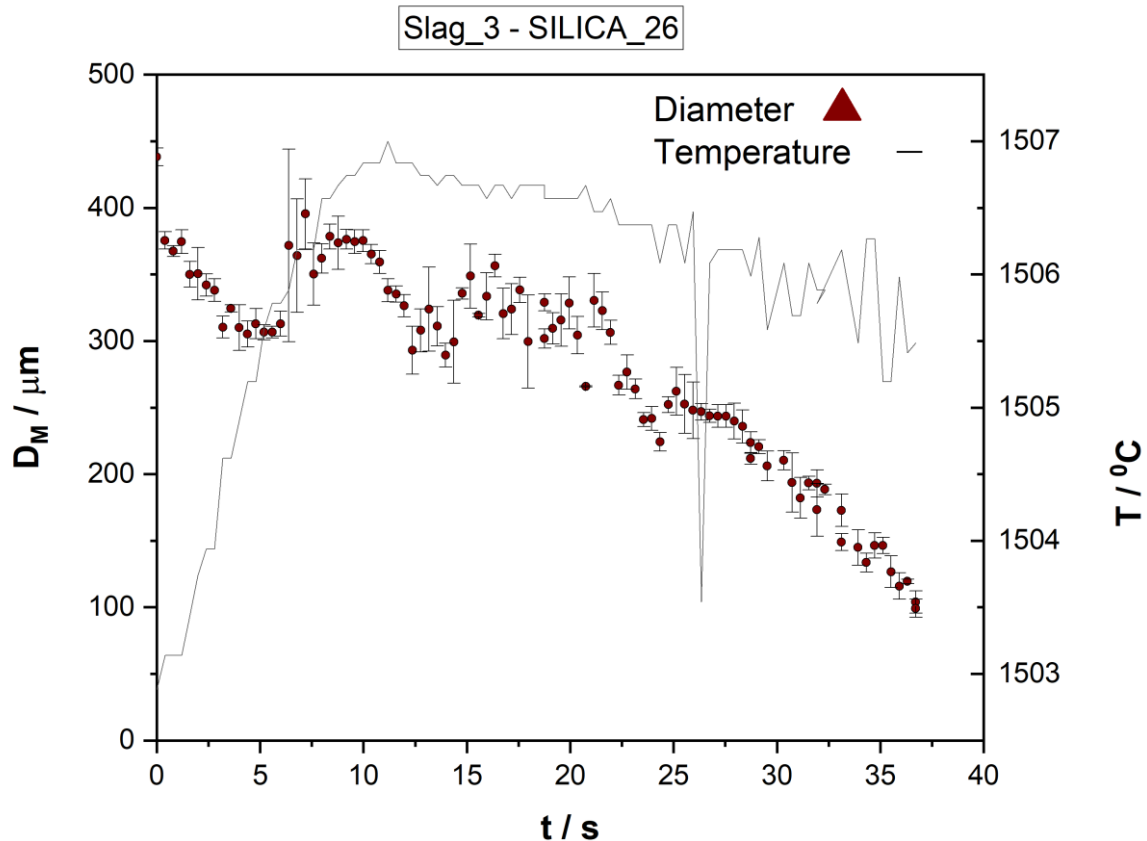


Figure 18: The dissolution profile of silica in SLAG 3

3.5.2 COMPUTATIONAL ANALYSIS

A Python script is created to set up the model and run the simulations. The effect of system parameters on the dissolution kinetics (which influenced the dissolution profile of the dissolving spherical oxide particles) is investigated with the aid of the Python routine. The change in the morphology of the particle is calculated over a period, with an initial radius taken from the onset of the dissolution process.

The modelling analysis of the different oxide particles in the slag samples is shown below.

ALUMINA: Multicomponent diffusion coefficient matrices were constructed for the dissolution of the alumina particle in the $\text{CaO-Al}_2\text{O}_3\text{-SiO}_2$ slag which is a three-component system. The chemical diffusion coefficients $D_{\text{CaO/CaO}}$, $D_{\text{CaO/Al}_2\text{O}_3}$, $D_{\text{Al}_2\text{O}_3/\text{CaO}}$, and $D_{\text{Al}_2\text{O}_3/\text{Al}_2\text{O}_3}$ used for the simulation of the oxide particle dissolution are given in Table 5 below.

Table 5. Diffusion Coefficient Matrix for the dissolution of alumina in the samples of the CaO-Al₂O₃-SiO₂ system.

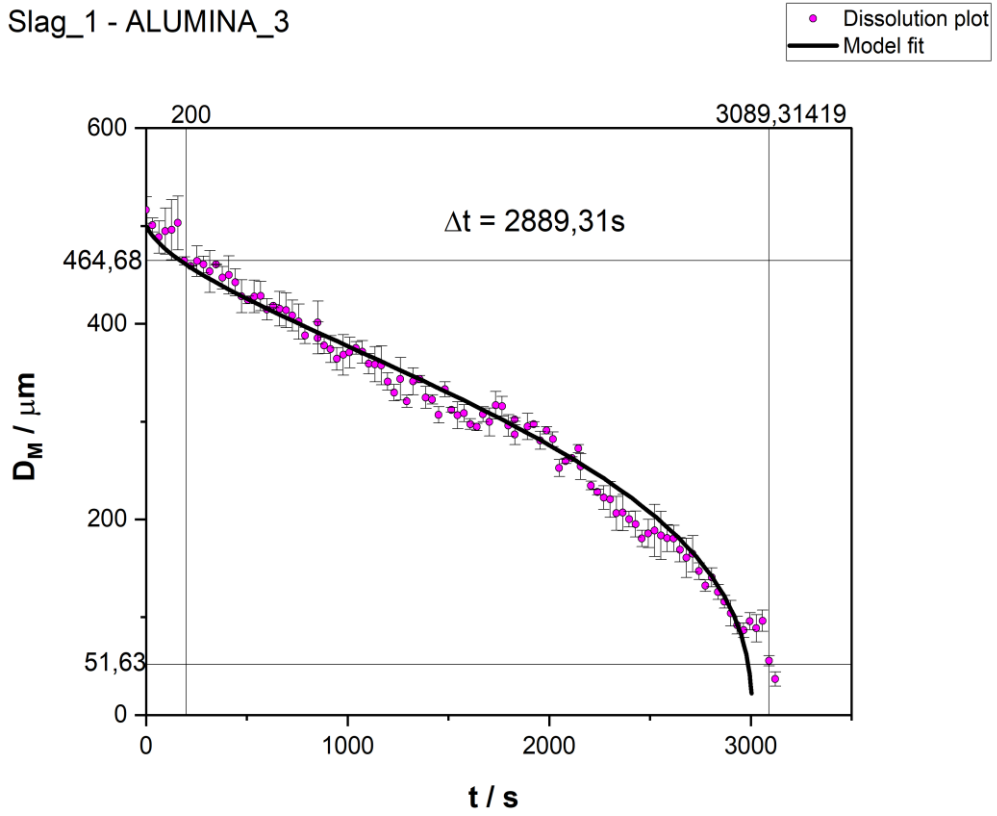
SLAG	D_{CaOCaO} / m^2s^{-1}	$D_{CaOAl_2O_3} / m^2s^{-1}$	$D_{Al_2O_3 CaO} / m^2s^{-1}$	$D_{Al_2O_3Al_2O_3} / m^2s^{-1}$
1	$7.67 \cdot 10^{-12}$	$-0.8 \cdot 10^{-12}$	$-0.98 \cdot 10^{-12}$	$2.62 \cdot 10^{-12}$
2	$5.08 \cdot 10^{-12}$	$-0.53 \cdot 10^{-12}$	$-0.65 \cdot 10^{-12}$	$1.73 \cdot 10^{-12}$
3	$70.39 \cdot 10^{-12}$	$-7.7 \cdot 10^{-12}$	$-9.45 \cdot 10^{-12}$	$25.2 \cdot 10^{-12}$

The solid line in Figure 19 (a-c) represents the calculated time-dependent radius of the alumina particle during dissolution which is a non-equilibrium process. As stated in the assumptions behind the numerical modelling approach given in Section 2.2, the diffusion coefficient of the solid particle is not constant in varying liquid oxide melt and the overall dissolution rate is influenced by the diffusion of cations through the interface. This is because cations have a different mobility rate in the slag melt which is a multi-component system, and this results in the diffusion profile deviating from a linear line.

It can be observed that the model fit shares a similar characteristic curvature as the results obtained from the dissolution experiments. The profile of the dissolution plot and the model in SLAG 1 shows a profile exhibiting an “S” shape while that of SLAG 2 and 3 is steeper, and they have a faster characteristic dissolution time (2120.8s and 607.7s). Also, SLAG 3 has the highest dissolution coefficient, followed by SLAG 1 and then, SLAG 2. The observed discrepancy was within the limit of error and could be ascribed to variation emanating from particle size analysis of the extracted image sequence.

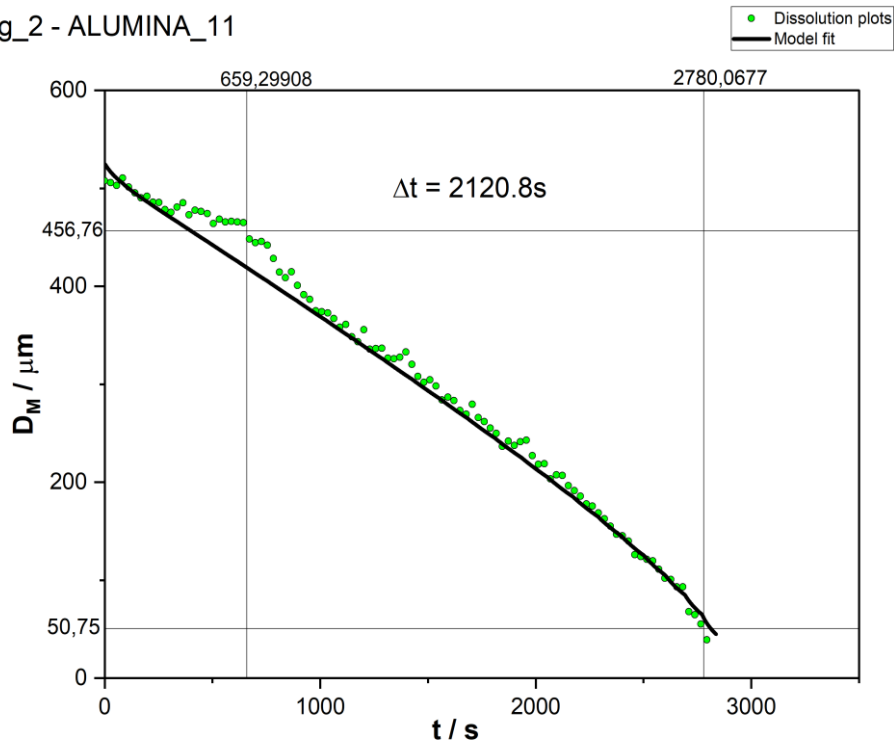
It can be concluded that diffusion is the rate-determining process during oxide particle dissolution in tested slag samples.

Slag_1 - ALUMINA_3

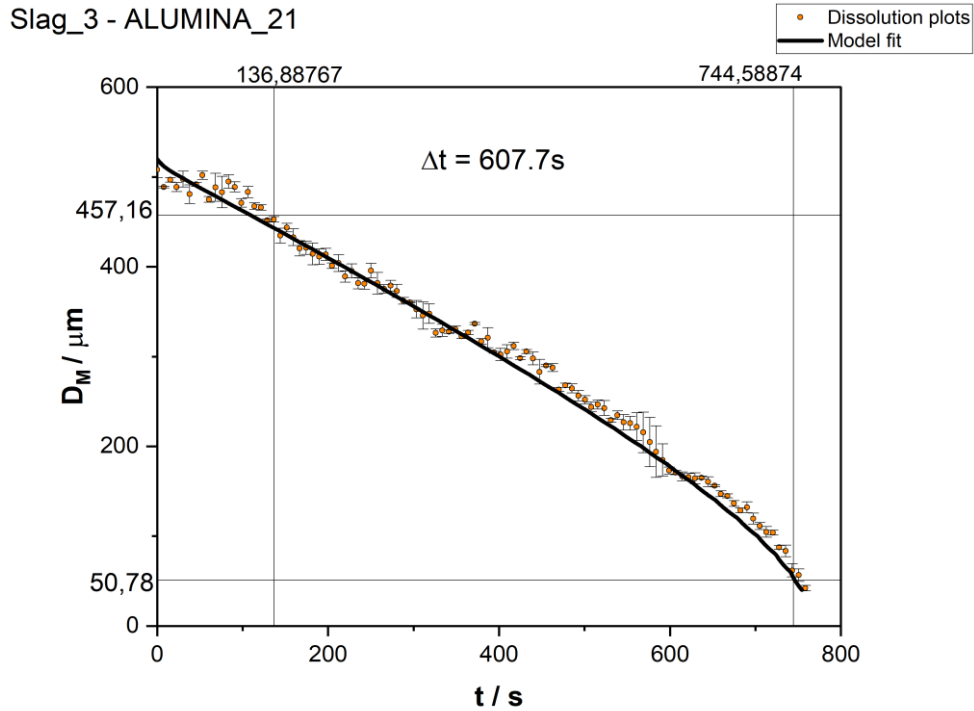


(a)

Slag_2 - ALUMINA_11



(b)



(c)

Figure 19: Mean particle diameter D_M versus dissolution time for alumina particles in (a) slag 1 (b) slag 2 and (c) slag 3. The coloured dots with error bars are from experimental observations. The black solid curves are the simulated results. The insert Δt is the characteristic dissolution time.

MA SPINEL

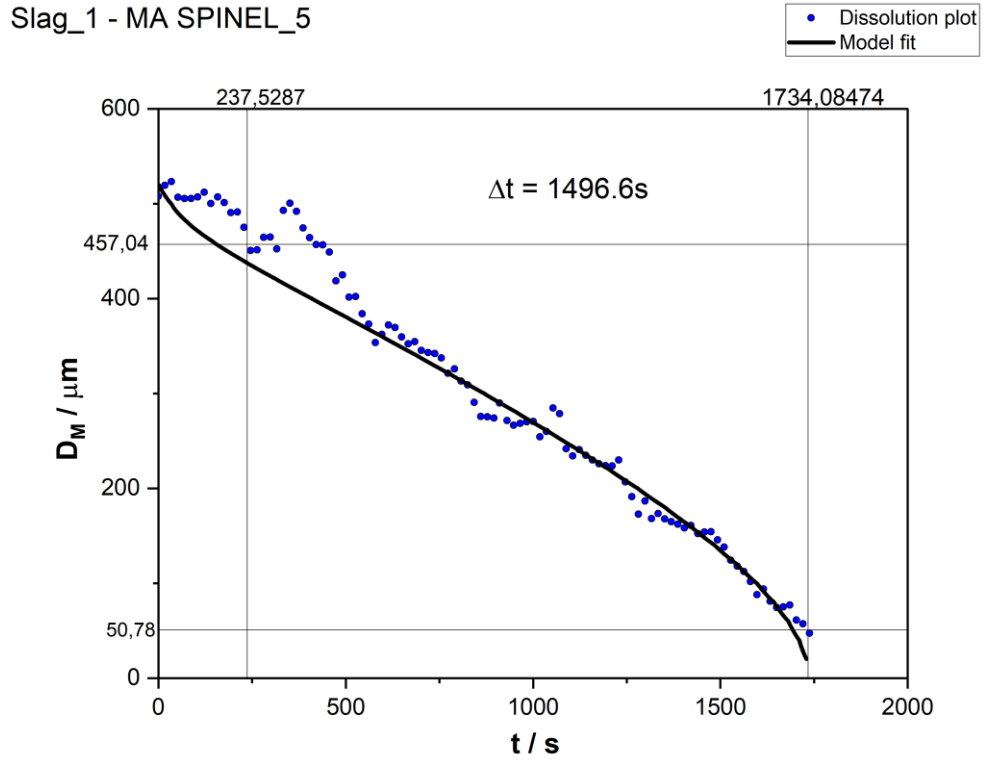
Table 6 shows the chemical diffusion coefficients $D_{\text{CaO}\text{CaO}}$, $D_{\text{CaOAl}_2\text{O}_3}$, $D_{\text{Al}_2\text{O}_3\text{CaO}}$, and $D_{\text{Al}_2\text{O}_3\text{Al}_2\text{O}_3}$ in the multicomponent diffusion coefficient matrices created for the dissolution of the MA spinel particle in the CaO-Al₂O₃-SiO₂ slag.

Table 6. Diffusion Coefficient Matrix for the dissolution of MA spinel in the 3-Component (CaO-Al₂O₃-SiO₂) system with a diffusion coefficient of $D_c = D \times 10^{-12} \text{ m}^2/\text{s}$.

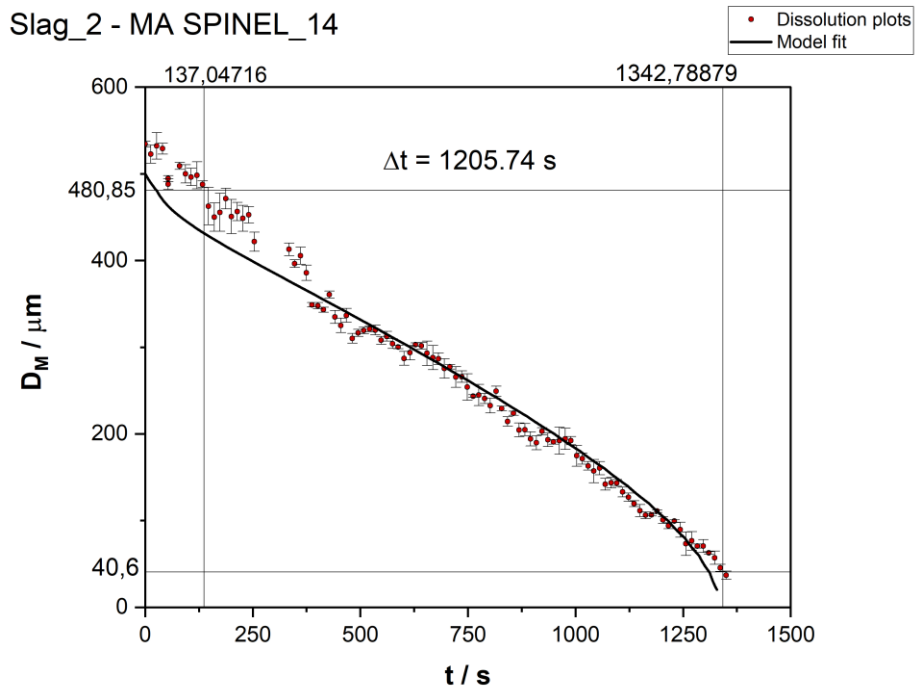
SLAG	$D_{\text{CaO}\text{CaO}} / \text{m}^2\text{s}^{-1}$	$D_{\text{CaOAl}_2\text{O}_3} / \text{m}^2\text{s}^{-1}$	$D_{\text{Al}_2\text{O}_3\text{CaO}} / \text{m}^2\text{s}^{-1}$	$D_{\text{Al}_2\text{O}_3\text{Al}_2\text{O}_3} / \text{m}^2\text{s}^{-1}$
1	$5.02 \cdot 10^{-12}$	$-0.52 \cdot 10^{-12}$	$-0.64 \cdot 10^{-12}$	$1.71 \cdot 10^{-12}$
2	$3.98 \cdot 10^{-12}$	$-0.42 \cdot 10^{-12}$	$-0.51 \cdot 10^{-12}$	$1.36 \cdot 10^{-12}$
3	$25.6 \cdot 10^{-12}$	$-2.67 \cdot 10^{-12}$	$-3.27 \cdot 10^{-12}$	$8.73 \cdot 10^{-12}$

The calculated model fit showed the same characteristic curvature as the experimental results for the dissolution of MA spinel in SLAG 3, however for the dissolution of these particles in SLAG 1 and 2 the simulated curves deviated significantly from the experimental

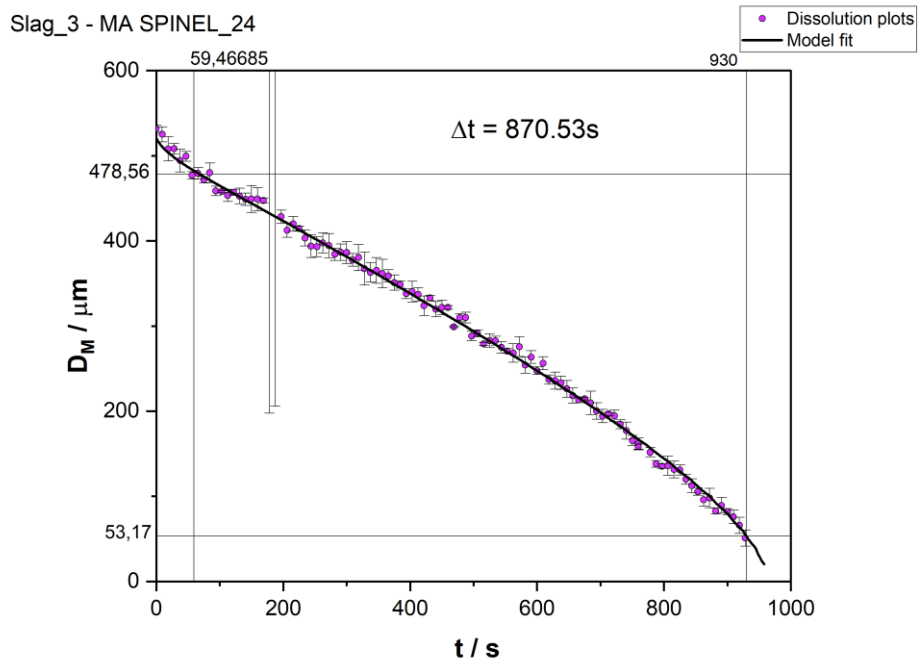
results. An examination of the profile of the dissolution plot and the model fit of the alumina particle in SLAG 1-3 showed that the characteristic dissolution time decreased from SLAG 1 to SLAG 3 (from 1496.6s, 1205.74s, to 870.53s).



(a)



(b)



(c)

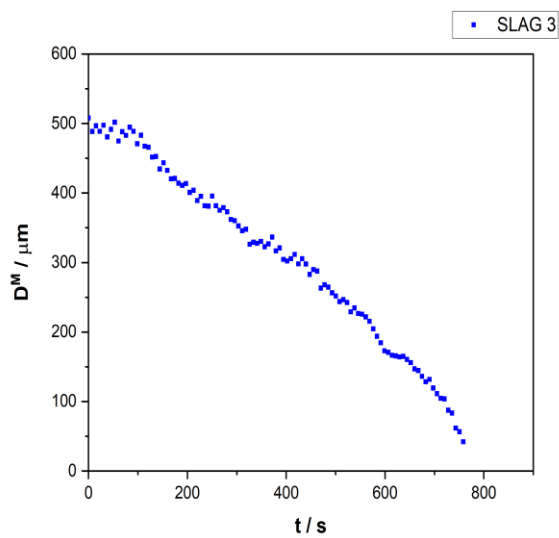
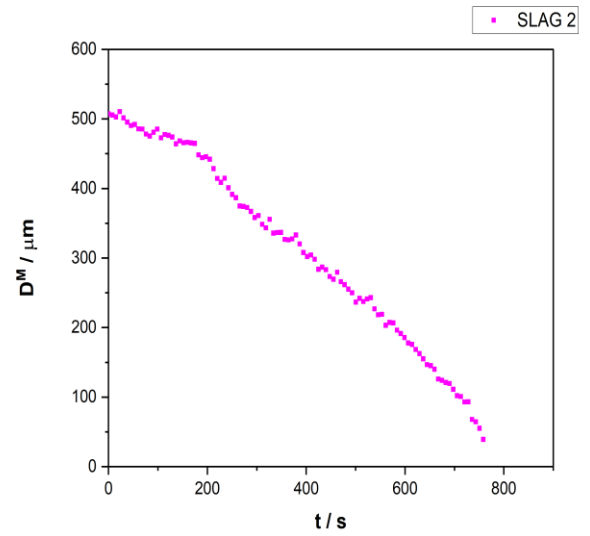
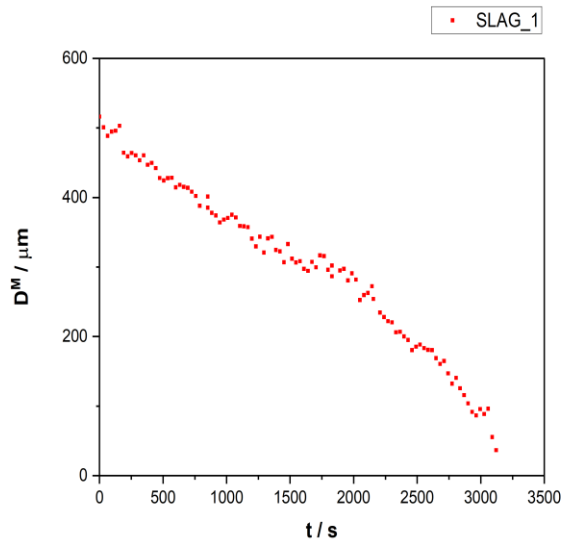
Figure 20: Mean particle diameter D_M versus dissolution time for MA spinel particles in (a) slag 1 (b) slag 2 and (c) slag 3. The coloured dots with error bars are from experimental observations. The black solid curves are the simulated results. The insert Δt is the characteristic dissolution time.

Chapter 4: CONCLUSIONS AND OUTLOOK

In this research, the dissolution of oxide particles was observed in slags of varying compositions, and the results are summarized as follows:

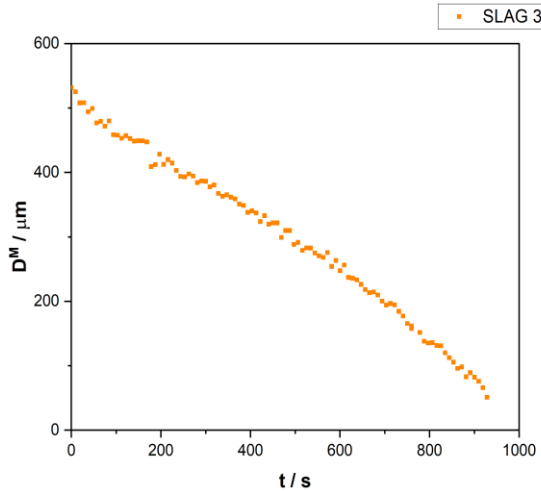
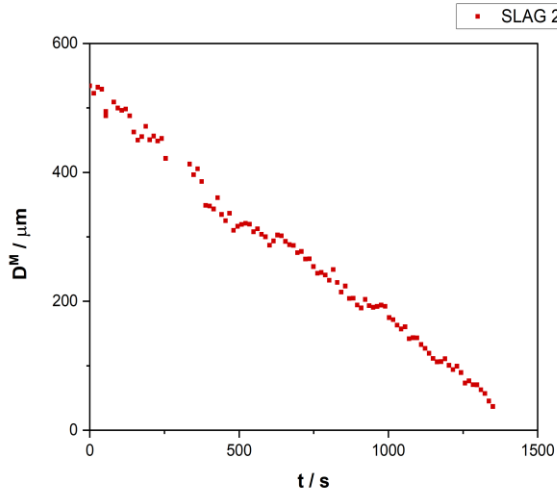
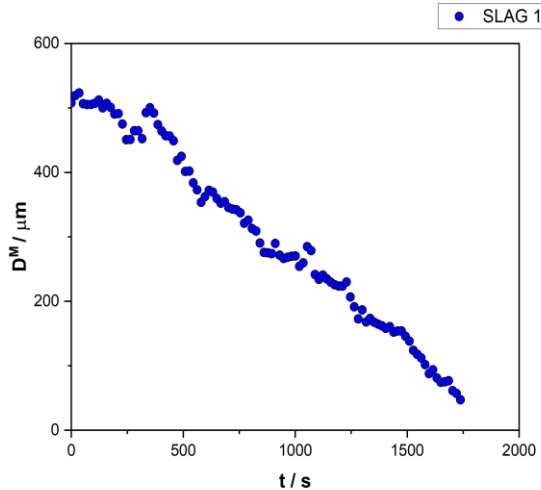
- The oxide particles were observed to be spherical, and it is likely that they maintained their spherical shape until complete dissolution. There was the observation of little or no particle rotation.
- Gas evolution led to measurement errors, which could be seen as data scatter in the dissolution profile, especially in the dissolution of the MA spinel particle in Slag 1.
- No sufficient prediction of the behavior of the characteristic diffusion time can be made from considering only the number of network-formers of the liquid slag. While the characteristic dissolution time for every particle is reduced from SLAG 1, SLAG 2 to SLAG 3, the characteristic dissolution time is not necessarily determined by the basicity of the slag. The slag sample had a basicity of 0.417, 0.778, and 0.571, and there was no distinct trend that was observed that could be attributed to this parameter, based on experimental test and the modelling fit. This reasoning indicates that a profound thermodynamic analysis is important to predict the dissolution behavior of oxide particle in molten slags.
- No boundary phase could be observed evolving during the dissolution of the oxide particles with the HT-LSCM.
- Also, it was observed that silica had the average fastest dissolution time while the alumina particle had the slowest and more uniformly dissolution profile.
- An examination of the profile of the dissolution plot and the model fit of the alumina and MA spinel particles in SLAG 1-3 showed that there was a consistent reduction in the characteristic dissolution time from SLAG 1 to SLAG 3 in both particles.
- The effect of oxide particles' porosity and thermal conductivity on the dissolution rate was not investigated and this might be the subject of future investigation.
- Further experiments and quantitative analyses of the dissolution of oxide particles in oxide melts of a different composition (which simulate the actual steelmaking process) may lead to the development of better refractory materials and innovation in the area of inclusion metallurgy.

Appendix



ALUMINA

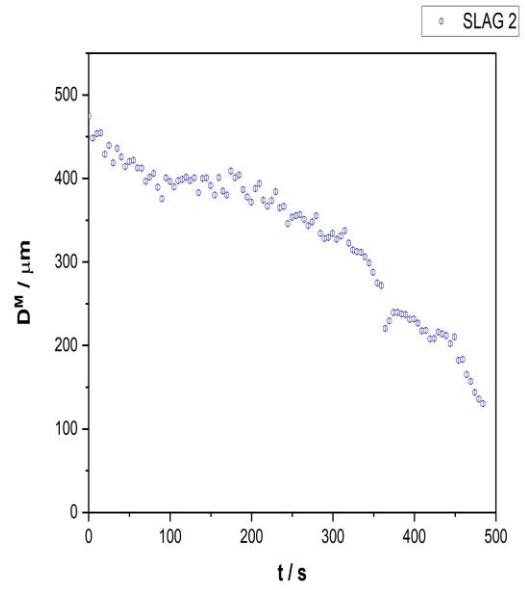
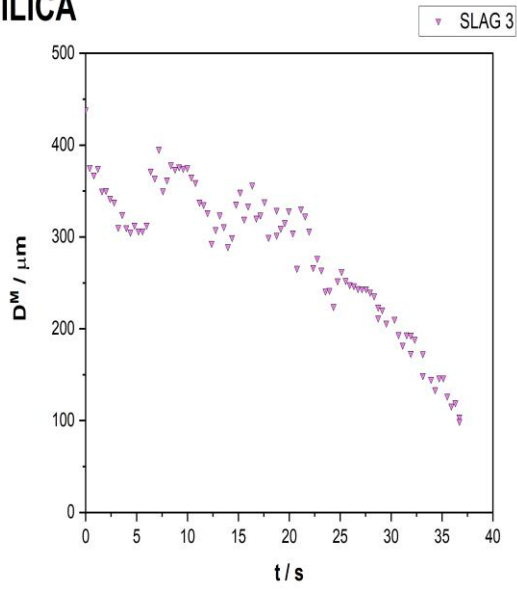
- I. Merged plots for the dissolution of the alumina particle in Slag 1-3.



MA SPINEL

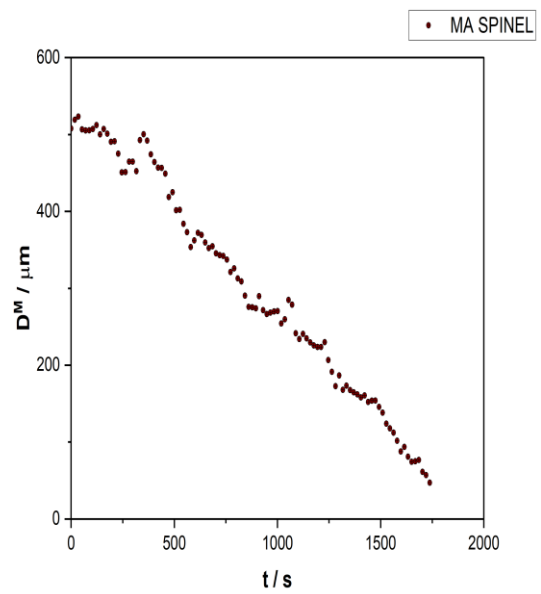
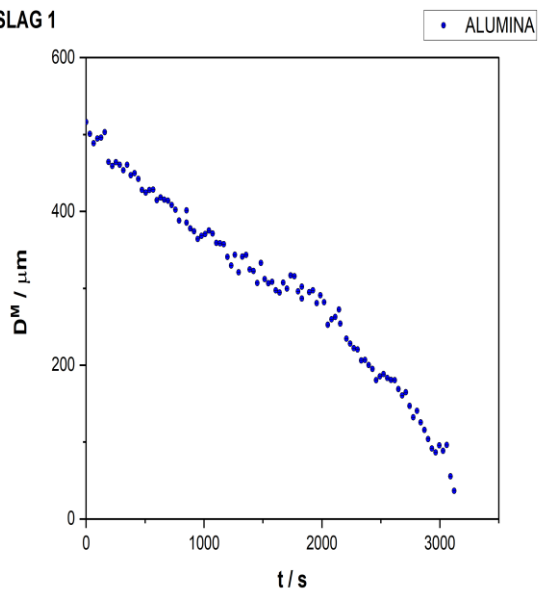
II. Merged plots for the dissolution of the MA spinel particle in Slag 1-3.

SILICA

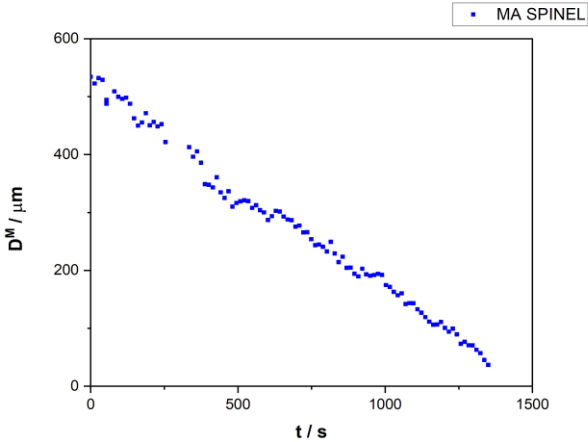
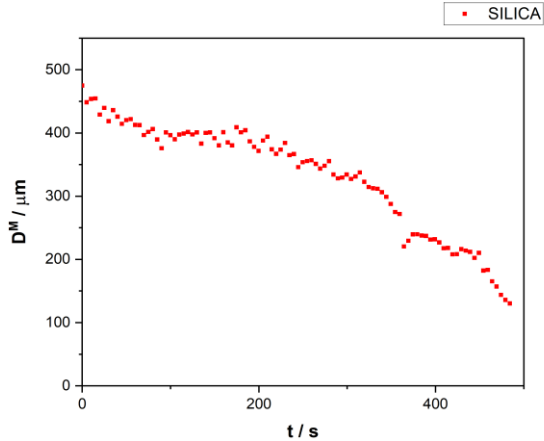
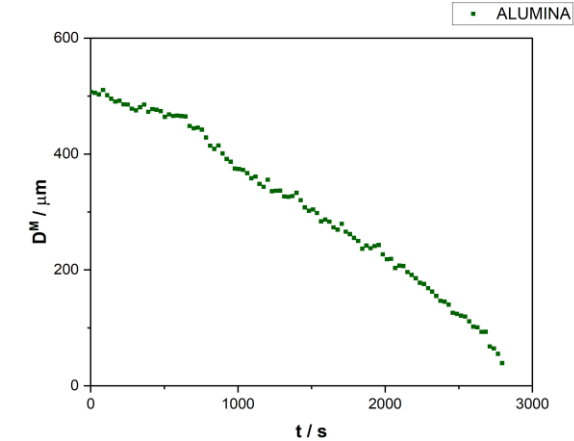


III. Merged plots for the dissolution of the silica particle in Slag 2-3.

SLAG 1

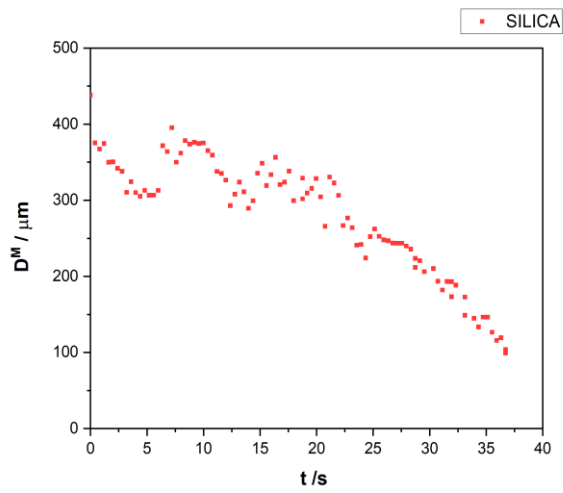
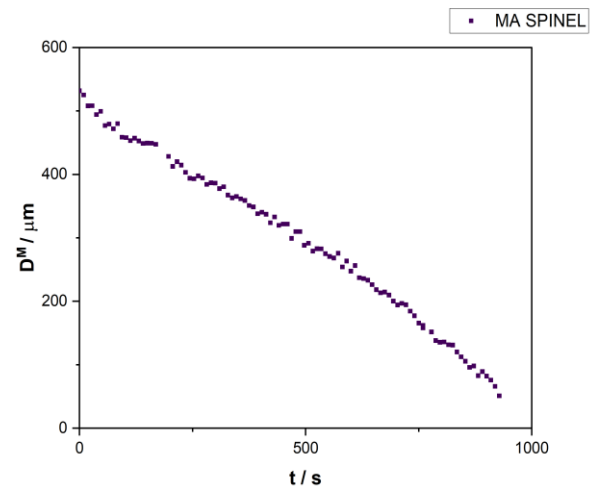
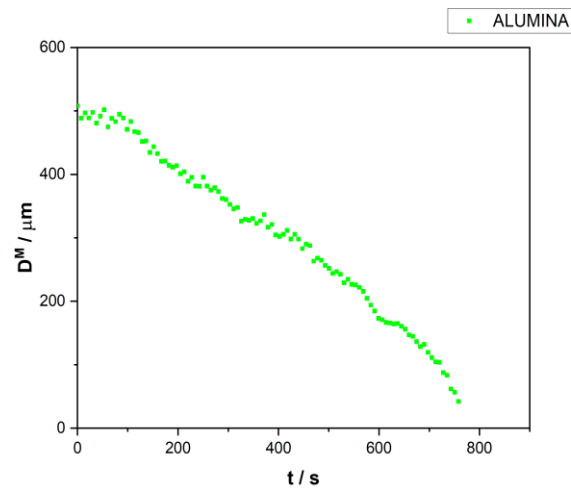


IV. Merged plots for the dissolution of the alumina and MA spinel particles in Slag 1.



SLAG 2

V. Merged plots for the dissolution of the alumina, silica, and MA spinel particles in Slag 2.



SLAG 3

VI. Merged plots for the dissolution of the alumina, silica and MA spinel particles in Slag 3.

Bibliography

1. Gerres, T., Lehne, J., Gökce M., Schenk, S., Swalec C., *Green steel production: How G7 countries can help change the global landscape*, Leadership Group for Industry Transition, 10 June 2021, <https://www.industrytransition.org/insights/g7-green-steel-production/>
2. International Energy Agency, *Iron and Steel Technology Roadmap: Part of Energy Technology Perspectives, Technology report — October 2020*, <https://www.iea.org/reports/iron-and-steel-technology-roadmap>.
3. Piemonti, A.; Conforti, A.; Cominoli, L.; Sorlini, S.; Luciano, A.; Plizzari, G.; *Use of Iron and Steel Slags in Concrete: State of the Art and Future Perspectives*. Sustainability 2021, 13, 556. <https://doi.org/10.3390/su13020556>
4. European Commission, 2030 climate & energy framework. https://ec.europa.eu/clima/eu-action/climate-strategies-targets/2030-climate-energy-framework_en
5. Worrell, E. and Carreon, J.R.; 2017. *Energy demand for materials in an international context*. Phil. Trans. R. Soc. A.3752016037720160377, <http://doi.org/10.1098/rsta.2016.0377>
6. WorldSteel Association. Available online: <https://www.worldsteel.org/> (accessed on 16 December 2021).
7. Recovery newsletter, *Valuable by-products: Slag recycling*, 02/2020, [Slag recycling - recovery \(recovery-worldwide.com\)](http://recovery-worldwide.com) Wang, Q.; Yan, P.; Han, S.; *The influence of steel slag on the hydration of cement during the hydration process of complex binder*. Sci. China Ser. E Technol. Sci. 2011, 54, 388–394.
8. Zhang, T.S.; Liu, F.T.; Liu, S.Q.; Zhou, Z.H.; Cheng, X.; *Factors influencing the properties of a steel slag composite cement*. Adv. Cem. Res. 2008, 20, 145–150.
9. Maruoka, Nobuhiro & Ito, Akihisa & Hayasaka, Miho & Nogami, Hiroshi. (2017). *Effect of CO2 Content in Quicklime on Dissolution Rate of Quicklime in Steelmaking Slags*. ISIJ International. 57. 1684-1690. 10.2355/isijinternational.ISIJINT-2017-261.
10. Lee, W.E. and Zhang, S. *Direct and indirect slag corrosion of oxide and oxide-c refractories. VII International Conference on Molten Slags Fluxes and Salts*, The South African Institute of Mining and Metallurgy, 2004.
11. H. Kimura, T. Yanagase, F. Noguchi, Y. Ueda, *Studies on the mechanism of CaO dissolution into slag melts*, Nippon Kinzoku Gakkaishi, 38 (1974), pp. 226-232
12. M. Valdez, K. Prapakorn, S. Sridhar, A.W. Cramb, *Dissolution of inclusions in steelmaking slags*, Proceedings of the ISSTech 2003 Conference (2003), pp. 789-798
13. Y. Satyoko, W.E. Lee, *Dissolution of dolomite and doloma in silicate slag*, Br. Ceram. Trans., 98 (6) (1999), pp. 261-265.
14. Bes A., *Dynamic Process Simulation of Limestone Calcination in Normal Shaft Kilns*, PhD dissertation, 2006. Belyaev, S.V., *Fundamentals of metallurgical and foundry production: students manual* (2016), pp. 211. Martinsson, J., Glaser, B. & Sichen, D. *Lime Dissolution in Foaming BOF Slag*. Metall Mater Trans B. 49, 3164–3170 (2018). <https://doi.org/10.1007/s11663-018-1421-6>
15. Belyaev, S.V., *Fundamentals of metallurgical and foundry production: students manual* (2016), pp. 211
16. Martinsson, J., Glaser, B. & Sichen, D., *Lime Dissolution in Foaming BOF Slag*. Metall Mater Trans B. 49, 3164–3170 (2018). <https://doi.org/10.1007/s11663-018-1421-6>
17. Kim S.J., Takekawa J., Shibata H., Kitamura S., Yamaguchi K. (2013), *Influence of slag basicity and temperature on Fe and Mn distribution between liquid Fe-Mn-Ca-O-S Matte and Molten Slag*. ISIJ Int 53(10):1715–1724
18. Moiseev, G.K., Vatolin, N.A., *Thermodynamic modeling: concentration, application, examples*. Rasplavy 5, 15–40 (1990).

-
19. Jonas T., Giuseppe D., Yaoming M., *A lattice Boltzmann method for immiscible two-phase Stokes flow with a local collision operator*, Computers & Mathematics with Applications, Volume 65, Issue 6, 2013, Pages 864-881, ISSN 0898-1221, <https://doi.org/10.1016/j.camwa.2012.05.018>.
 20. Zhou, J.G. *Macroscopic Lattice Boltzmann Method*. Water 2021, 13, 61. <https://doi.org/10.3390/w13010061>
 21. Verhaeghe, F. & Arnout, S. & Blanpain, B. & Wollants, P. (2006). *Lattice-Boltzmann Modeling of Dissolution Phenomena*. Physical review. E, Statistical, nonlinear, and soft matter physics. 73. 036316. <https://doi.org/10.1103/PhysRevE.73.036316>.
 22. Alihussein, H., 2020. *Massively parallel simulations of chemical dissolution in porous media based on advanced lattice Boltzmann models*. <https://doi.org/10.24355/dbbs.084-202012031014-0>
 23. McNamara, G.R. & Zanetti, G. (1988). *Use of the Boltzmann Equation to Simulate Lattice-Gas Automata*. Physical review letters. 61. 2332-2335. <http://doi.org/10.1103/PhysRevLett.61.2332>.
 24. Y. Xuan, K. Zhao, Q. Li; *Investigation on mass diffusion process in porous media based on Lattice Boltzmann method*. Int. J. Heat Mass Tran., 46 (10) (2010), pp. 1039-1051.
 25. Adrian R.G. Harwood, Alistair J. Revell, "Parallelisation of an interactive lattice-Boltzmann method on an Android-powered mobile device", Advances in Engineering Software, Volume 104, 2017, Pages 38-50, ISSN 0965-9978, <https://doi.org/10.1016/j.advengsoft.2016.11.005>.
 26. Alihussein, H., 2020. *Massively parallel simulations of chemical dissolution in porous media based on advanced lattice Boltzmann models*. <https://doi.org/10.24355/dbbs.084-202012031014-0>
 27. Aursjø, O. & Pride, S. (2015). *Lattice Boltzmann method for diffusion-limited partial dissolution of fluids*. Physical Review E. 92. 013306. <http://doi.org/10.1103/PhysRevE.92.013306>.
 28. Y. Xuan, K. Zhao, Q. Li; *Investigation on mass diffusion process in porous media based on Lattice Boltzmann method*. Int. J. Heat Mass Tran., 46 (10) (2010), pp. 1039-1051.
 29. Keijo M., Jari H., Jussi T., Tuomo R., *Comparison of implementations of the lattice-Boltzmann method*, Computers & Mathematics with Applications, Volume 55, Issue 7, 2008, Pages 1514-1524, ISSN 0898-1221, <https://doi.org/10.1016/j.camwa.2007.08.001>.
 30. Zagvozdina, K. & Burovski, E. (2021). *Exploring the accuracy of the Lattice Boltzmann method*. Journal of Physics: Conference Series. 1740. 012027. <http://doi.org/10.1088/1742-6596/1740/1/012027>.
 31. Huidan Y., Xi C., Zhiqiang W., Debanjan D., Everton L., Ye Z., and Shawn D.T. *Mass-conserved volumetric lattice Boltzmann method for complex flows with wilfully moving boundaries*, Phys. Rev. E 89, 063304 – Published 11 June 2014, Vol. 89, Iss. 6 — June 2014
 32. Zheng, J. (2018). *The new direction of computational fluid dynamics and its application in industry*. Journal of Physics: Conference Series. 1064. 012060. <http://doi.org/10.1088/1742-6596/1064/1/012060>.
 33. Li Q, Luo K.H., Kang Q.J., He Y.L., Chen Q., Liu Q. *Lattice Boltzmann Methods for Multiphase Flow and Phase-Change Heat Transfer*. Prog Energy Combust Sci (2016) 52:62–105. <http://doi.org/10.1016/j.pecs.2015.10.001>
 34. Guo Z, Shu C. *Lattice Boltzmann Method and its Applications in Engineering*. Singapore, Singapore: World Scientific Publisher (2013). Vol. 3, p. 25–8.
 35. Wang, Y.; Yang, L.; Shu, C. *From Lattice Boltzmann Method to Lattice Boltzmann Flux Solver*. Entropy 2015, 17, 7713-7735. <https://doi.org/10.3390/e17117713>

36. Zhang, Y., Guang, P. and Qiaogao, H. "ICCM2016: The Implementation of Two-Dimensional Multi-Block Lattice Boltzmann Method on GPU." *International Journal of Computational Methods* (2019).
37. He, X., Luo, L.S. *Lattice Boltzmann Model for the Incompressible Navier–Stokes Equation*. *Journal of Statistical Physics* 88, 927–944 (1997).
<https://doi.org/10.1023/B:JOSS.0000015179.12689.e4>
38. Verhaeghe, Frederik & Arnout, Sander & Blanpain, Bart & Wollants, Patrick. (2005). *Lattice Boltzmann Model for Diffusion-Controlled Dissolution of Solid Structures in Multicomponent Liquids*. *Physical review. E, Statistical, nonlinear, and soft matter physics*. 72. 036308. <https://doi.org/10.1103/PhysRevE.72.036308>.
39. Cogswell, D. (2010). *A phase-field study of ternary multiphase microstructures*. PhD thesis.
40. R. S. Qin & H. K. Bhadeshia (2010), *Phase field method*, *Materials Science and Technology*, 26:7, 803-811, <https://doi.org/10.1179/174328409X453190>
41. Liu, J. & Zou, J. & Guo, M. & Moelans, N. (2016). *Phase field simulation study of the dissolution behavior of Al₂O₃ into CaO- Al₂O₃-SiO₂ slags*. *Computational Materials Science*. 119. <http://10.1016/j.commatsci.2016.03.034>.
42. Singh R.Y. & Kanth, G. (2013). *Phase Field Modeling of Microstructure Evolution During Phase Transformations in Materials*.
43. LeVeque, R.J., *Finite difference methods for ordinary and partial differential equations: Steady-state and time-dependent problems*, SIAM, Philadelphia, 2007.
44. Sandip Mazumder, *Numerical Methods for Partial Differential Equations: Finite Difference and Finite Volume Methods*; <http://dx.doi.org/10.1016/B978-0-12-849894-1.00001-9>
45. Ogris, M, E. Gamsjäger: "Numerical treatment of oxide particle dissolution in multicomponent slags with local Gibbs energy minimization", submitted to *Steel Research International*, (2022).
46. Pelton, A.D., Degterov, S.A., Eriksson, G., Robelin, C. and Dessureault, Y., 2000. *The modified quasichemical model I—binary solutions*. *Metallurgical and Materials Transactions B*, 31(4), pp.651-659.
47. Pelton, A.D., 2001. *A general "geometric" thermodynamic model for multicomponent solutions*. *Calphad*, 25(2), pp.319-328.
48. Chartrand, P. and Pelton, A.D., 2000. *On the choice of "geometric" thermodynamic models*. *Journal of phase equilibria*, 21(2), pp.141-147.
49. V. Kircher, Burhanuddin, H. Harmuth, *Design, operation and evaluation of an improved refractory wear testing technique*, *Measurement*, Volume 178, 2021, 109429, ISSN 0263-2241, <https://doi.org/10.1016/j.measurement.2021.109429>.
50. M. Matsushima, S. Yaadoomaru, K. Mori, Y. Kawai, *A Fundamental Study on the Dissolution Rate of Solid Lime into Liquid Slag*, *Transactions of the Iron and Steel Institute of Japan*, 1977, Volume 17, Issue 8, Pages 442-449, Released December 24, 2019, Online ISSN 1881-1183,
<https://doi.org/10.2355/isijinternational1966.17.442>
51. Wenwen Mao, Chenxiao Li, Hua Lu, Hong Li & Wei Xie (2018), *Limestone dissolution and decomposition in steelmaking slag*, *Ironmaking & Steelmaking*, 45:8, 720-726,
<http://10.1080/03019233.2017.1326549>
52. Keiji O., *Model Experiment for Acceleration of Lime Dissolution into Slag under Ultrasound Irradiation Conditions*, *ISIJ International*, 2017, Volume 57, Issue 10, Pages 1691-1697, Released October 17, 2017,
<https://doi.org/10.2355/isijinternational.ISIJINT-2017-208>.
53. Chikama, H., Shibata, H., Emi, T. and Suzuki, M., *In situ real time observation of planar to cellular and cellular to dendritic transition of crystals growing in Fe–C alloy melts*. *Mater. T. JIM*, 1996, 37(4), 620–626

-
54. Keiji O., *Model Experiment for Acceleration of Lime Dissolution into Slag under Ultrasound Irradiation Conditions*, ISIJ International, 2017, Volume 57, Issue 10, Pages 1691-1697, Released October 17, 2017, <https://doi.org/10.2355/isijinternational.ISIJINT-2017-208>.
 55. Guo, Xiaoling & Guo, M. & Sun, Z.H.I. & Van Dyck, Joris & Blanpain, Bart & Wollants, Patrick. (2010). *Chemical dissolution of lime particles in CaO-Al₂O₃-SiO₂-based slags: An in-situ observation approach*. Materials Science and Technology Conference and Exhibition 2010, MS and T'10. 3. 1739-1750.
 56. Fuchs, N.; Bernhard, C.; Michelic, S.; Dippenaar, Rian. (2020). *HT-LSCM as a Tool for Indirect Determination of Precipitates by Real-Time Grain Growth Observations*. 10.1007/978-3-030-36296-6_5.
 57. Department of Metallurgy, Montanuniversität Leoben, *In-situ observation by HT-LSCM*, <https://metallurgy.at/en/4-high-temperature-laser-scanning-microscope-ht-lscm/>
 58. Mu, W., Hedström, P., Shibata, H. et al. Mu, W., Hedström, P., Shibata, H. et al. *High-Temperature Confocal Laser Scanning Microscopy Studies of Ferrite Formation in Inclusion-Engineered Steels: A Review*. JOM 70, 2283–2295 (2018). <https://doi.org/10.1007/s11837-018-2921-1>
 59. Product Data Sheet, Available at: [comparison_table.pdf \(sandoz.ch\)](#)
 60. VirtualDub, Version 1.9.10, developed by A. Lee. Available at: <http://www.virtualdub.org>
 61. Jens Rüdigs Makroaufmaßprogramm <http://ruedig.de/tmp/messprogramm.htm>